# Estimating fixed nitrogen loss and associated isotope effects using concentration and isotope measurements of $NO_3^-$, $NO_2^-$, and $N_2$ from the Eastern Tropical South Pacific oxygen deficient zone

Brian Peters[1], Rachel Horak[2], Alan Devol[2], Clara Fuchsman[2], Matthew Forbes[1], Calvin W. Mordy[3,4], and Karen L. Casciotti[1*]

[1]Department of Earth System Science, Stanford University, 473 Via Ortega, Stanford, CA 94303, USA

[2] School of Oceanography, University of Washington, Seattle WA 98105, USA

[3] Joint Institute for the Study of the Atmosphere and Ocean, Box 355672, University of Washington, Seattle, WA 98105-5672, USA

[4] Pacific Marine Environmental Laboratory, NOAA, 7600 Sand Point Way, NE, Seattle WA 98115, USA

*corresponding author

kcasciotti@stanford.edu

650-721-5545

**Abstract**

Quantifying the pathways of fixed nitrogen (N) loss in marine oxygen deficient zones (ODZs) and the isotopic fractionation caused by these processes are important for understanding the marine fixed N budget and its potential for change. In this study, a variety of approaches were used to quantify fixed N loss in the eastern tropical South Pacific Ocean (ETSP). The required measurements included nutrient concentration (nitrate—$NO_3^-$, nitrite—$NO_2^-$, and phosphate—$PO_4^{3-}$), gas ratio ($N_2$/Ar) measurements, and stable N and O isotopes in $NO_3^-$, $NO_2^-$, and nitrogen gas ($N_2$). The dissolved inorganic nitrogen deficit calculated from [$PO_4^{3-}$] ($[DIN]_{def,P}$) exceeded the concentration of $N_2$ gas biologically produced in the ODZ (local $[N_2]_{bio}$) throughout the ODZ at most stations, likely due to release of $PO_4^{3-}$ from sediments driving up $[DIN]_{def,P}$. Calculating DIN deficit using water mass analysis and local oxygen ($O_2$) consumption ($[DIN]_{def,OMP}$) yielded better agreement with local $[N_2]_{bio}$ than $[DIN]_{def,P}$, except at the maximum $[N_2]_{bio}$, where $[DIN]_{def,OMP}$ misses contributions of anaerobic ammonia oxidation (anammox) to $N_2$ production. We used the mismatch between $[DIN]_{def,OMP}$ and $[N_2]_{bio}$ to estimate a 29% contribution of anammox to $[N_2]_{bio}$. Stable isotopic measurements of $NO_2^-$, $NO_3^-$, and $N_2$ were used alongside $[N_2]_{bio}$ and new estimates of $[DIN]_{def}$ to calculate N and O isotope effects for $NO_3^-$ reduction ($^{15}\varepsilon_{NAR}$ and $^{18}\varepsilon_{NAR}$, respectively), and N isotope effects for DIN removal ($^{15}\varepsilon_{DIN\text{-}R}$). While the various methods for estimating $[DIN]_{def}$ had little effect on the isotope effects for DIN removal, differences between $^{15}\varepsilon_{NAR}$ and $^{15}\varepsilon_{DIN\text{-}R}$, and variations with depth in the ODZ were observed. Using a simple time-dependent ODZ model, we interpreted these patterns to reflect the influences of $NO_2^-$ oxidation and $NO_2^-$ accumulation on expression of isotopic fractionation in the ODZ.

## Introduction

The eastern tropical South Pacific Ocean (ETSP) is a region of high biological productivity, stimulated by upwelling of thermocline waters containing elevated nutrient concentrations (Chavez and Messie, 2009; Escribano et al., 2004; Stramma et al., 2010; Ulloa and Pantoja, 2009). Organic matter exported from the highly productive surface waters creates a high oxygen ($O_2$) demand at depth. When coupled to sluggish physical circulation, this supply of organic matter maintains a permanent $O_2$ deficient zone (ODZ) between $\sigma_\theta$ = 26.2 - 26.8 kg $m^{-3}$, which is roughly in the 200 m to 400 m depth range (Czeschel et al., 2011; Fuenzalida et al., 2009; Karstensen et al., 2008; Kessler, 2006; Paulmier et al., 2006; Paulmier et al., 2009; Stramma et al., 2010).

In the absence of $O_2$, many marine microorganisms can use dissimilatory nitrate ($NO_3^-$) reduction to oxidize organic matter (Cline and Richards, 1972; Codispoti and Christensen, 1985). Nitrite ($NO_2^-$), the product of $NO_3^-$ reduction, has been observed to accumulate in the ETSP ODZ, but it can be reoxidized to $NO_3^-$, or further reduced to nitrogen gas ($N_2$) by two mechanisms: 1) denitrification, the stepwise reduction of $NO_2^-$ to gaseous products nitric oxide (NO), nitrous oxide ($N_2O$) and $N_2$, and 2) anaerobic ammonium ($NH_4^+$) oxidation ('anammox') which oxidizes $NH_4^+$ to $N_2$ using $NO_2^-$. These two processes collectively lead to 'fixed N loss', whereby fixed N ($NO_3^-$, $NO_2^-$, $NH_4^+$) becomes less biologically available through conversion to gaseous products. Denitrification is a heterotrophic process that requires an input of organic matter. It produces $N_2O$ and $N_2$ from $NO_2^-$, as well as releasing carbon dioxide ($CO_2$), phosphate ($PO_4^{3-}$), and $NH_4^+$ from the respired organic matter (Cline and Richards, 1972; Codispoti and Christensen, 1985; Lipschultz et al., 1990; Koeve and Kähler, 2010). As $NO_2^-$ tends to accumulate in ODZs, the organic matter supply is commonly believed to be the limiting substrate for denitrification (Ward et al., 2008; Kalvelage et al., 2013; Babbin et al., 2014; Chang et al., 2014).

Anammox is an autotrophic process that consumes $CO_2$ while producing $N_2$ (Van de Graaf et al., 1996; Strous et al., 1998; Dalsgaard et al., 2003; Brunner et al., 2013). Only one N atom of the $N_2$ produced is derived from $NO_2^-$, while the other comes from $NH_4^+$. Because $NH_4^+$ does not typically accumulate in ODZs (Richards, 1965), anammox is limited by $NH_4^+$ in much of the ODZ where $NO_2^-$ accumulates. The relative importance of anammox and denitrification to fixed N loss are thus thought to be linked through organic matter stoichiometry (Koeve and

Kahler, 2010; Ward, 2013; Babbin et al., 2014) unless an alternate source of $NH_4^+$ is available, such as from dissimilatory $NO_3^-$ reduction to $NH_4^+$ (DNRA; Lam et al., 2009) organic matter degradation by sulfate reduction (Canfield et al., 2010) or zooplankton excretion (Bianchi et al., 2014). Decoupling of anammox and denitrification may also occur where bacterial $NO_2^-$ oxidation recycles $NO_2^-$ back to $NO_3^-$ (Peters et al., 2016; Penn et al., 2016; Babbin et al., 2017), allowing anammox to be responsible for a larger portion of $NO_2^-$ reduction. As denitrification and anammox have different implications for carbon and nitrogen cycling, and the relative importance appears to vary in space and time (Ward et al., 2009; Jensen et al., 2011; Dalsgaard et al., 2012), determining both the mechanism and controls of fixed N loss in ODZs remain important yet unresolved tasks.

One way to determine the amount of fixed N that has been removed from a region is to determine the concentration of $N_2$ that has been produced biologically ($[N_2]_{bio}$), using the ratios of $N_2$ to argon (Ar) dissolved in seawater. While this is the most direct way to calculate the quantity of fixed N that has been removed, these measurements are difficult to make. The amount of biogenic $N_2$ produced in ODZs (0 to ~40 μM) is quite small relative to the total amount of $N_2$ that is found in seawater (~400 to 500 μM at equilibrium), and it requires precise determination by mass spectrometry. Thus, it is more common to estimate fixed N removal by calculating the dissolved inorganic nitrogen deficit relative to $[PO_4^{3-}]$ ($[DIN]_{def,P}$), using Redfield stoichiometry (16N: 1P; Redfield et al., 1963) to predict the amount of DIN expected in a given water sample ($[DIN]_{exp,P}$). This is analogous to the tracer N*, which uses a ratio of 16N: 1P and includes a constant of 2.9 umol/kg to reach a global average N* near zero (Gruber and Sarmiento, 1997). In the ETSP, we used the background conditions and nutrient ratios reported by Chang et al. (2010) to derive $[DIN]_{exp,P}$:

$$[DIN]_{exp,P} = 15.8*([PO_4^{3-}] - 0.3) \quad (1)$$

$[DIN]_{def,P}$ was then calculated from the difference between the observed DIN concentration ($[DIN]_{obs}$) and $[DIN]_{exp,P}$:

$$[DIN]_{obs} = [NO_2^-] + [NO_3^-] + [NH_4^+] \quad (2)$$

$$[DIN]_{def,P} = [DIN]_{exp,P} - [DIN]_{obs} \quad (3)$$

As noted in equation 2, $NH_4^+$ can contribute to the observed DIN pool, but it is rarely observed in the water column of the ETSP ODZ away from the coast, and was below detection within the ODZ during this study (Peng et al., 2016; Babbin et al., 2017). The benefit of the $[DIN]_{def,P}$ method is that it relies on nutrient measurements, which are easier to perform and more widely available than $[N_2]_{bio}$ determinations. However, the remineralization ratio of N:P is known to vary spatially (Arrigo, 2005; Franz et al., 2012; Martiny et al., 2013). Furthermore, previous studies have demonstrated a preferential remineralization of N relative to P in the Eastern Tropical North Pacific (ETNP) ODZ (Van Mooy et al., 2002), suggesting remineralization stoichiometry may be even more variable in suboxic regions and may bias estimates of $N_2$ fixation or N loss (Mills and Arrigo, 2010; Mills et al., 2015). Given these uncertainties in N:P remineralization stoichiometry, some lack of agreement between $[DIN]_{def,P}$ and $[N_2]_{bio}$ might be expected.

While relatively good agreement between $[N_2]_{bio}$ measurements and corresponding $[DIN]_{def,P}$ values have been previously reported for the ETSP ODZ (Chang et al., 2010; Bourbonnais et al., 2015), slight mismatches between the two parameters have been identified. Chang et al. (2010) found that measurements of $[N_2]_{bio}$ roughly matched the $[DIN]_{def,P}$ in the upper and middle parts of the ETSP ODZ. However, the $[DIN]_{def,P}$ appeared to slightly underestimate $[N_2]_{bio}$ in the lower half of the ODZ. The authors proposed the mismatch between $[DIN]_{def,P}$ and $[N_2]_{bio}$ was likely due to a change in N:P remineralization stoichiometry or a shift in N loss mechanisms. A recent study by Bourbonnais et al. (2015) also found general agreement between $[N_2]_{bio}$ and $[DIN]_{def,P}$, although $[DIN]_{def,P}$ appeared to slightly exceed $[N_2]_{bio}$ at most sample depths in a near-shore eddy. A larger disagreement between $[DIN]_{def,P}$ and $[N_2]_{bio}$ was found by Hu et al. (2016), whereby the increase in $[DIN]_{def,P}$ was nearly double the corresponding $[N_2]_{bio}$ increase along the Peruvian shelf. The authors argued that release of $PO_4^{3-}$ from sediments to the water column could explain some of this mismatch, as the addition of $PO_4^{3-}$ from sediments would artificially increase $[DIN]_{def,P}$ if the $PO_4^{3-}$ release was not paralleled by a stoichiometric release of fixed N. Thus, the reliability of $[DIN]_{def,P}$ as an indicator of fixed N loss may need to be evaluated on a case-by-case basis.

The suitability of $[DIN]_{def,P}$ as a predictor of fixed N loss also has implications for interpreting the $NO_3^-$ isotope measurements in ODZs if the amount of N removed is over- or underestimated. The ratio of $^{15}N$ to $^{14}N$ in $NO_3^-$ is reported as $\delta^{15}N_{NO3} = (^{15}N/^{14}N_{NO3} \div {}^{15}N/^{14}N_{air} - 1)*10^3$ in units of ‰ versus atmospheric $N_2$ ('air'). $\delta^{15}N$ in $NO_3^-$ and $NO_2^-$ in ODZs respond to biogeochemical processes that fractionate stable isotopes according to specific isotope effects (e.g., for N isotopes, $^{15}\varepsilon = {}^{14}k/{}^{15}k$, where $^{14}k$ and $^{15}k$ are the first order rate constants for reaction of the light and heavy isotopes, respectively). Isotope effects arise due to small differences in the rates at which heavy and light isotope-containing molecules react, and laboratory-determined isotope effects for $NO_3^-$ reduction ($^{15}\varepsilon_{NAR}$), $NO_2^-$ reduction ($^{15}\varepsilon_{NIR}$), and $NO_2^-$ oxidation ($^{15}\varepsilon_{NXR}$) can be used to interpret the relative importance of those N cycle processes in ODZs (Casciotti et al., 2013, Buchwald et al., 2015; Peters et al., 2016). $\delta^{15}N_{NO3}$ measurements can also be used to obtain 'field' estimates, or apparent, $^{15}\varepsilon_{NAR}$ values. These might be expected to differ from the laboratory-derived estimates, since the expressed isotope effects may be dependent on the occurrence of specific microbial species, relative rates of individual steps in a multi-step process, supply of organic carbon and $NO_3^-$ (Krittee et al., 2012) or mixing and the extent of $NO_3^-$ removal in the ODZ (Deutsch et al., 2004). Further, $^{15}\varepsilon_{NAR}$, the isotope effect for $NO_3^-$ reduction can vary regionally and differ from $^{15}\varepsilon_{DIN\text{-}R}$, the isotope effect for DIN removal, due to the effects of co-occurring processes (Bourbonnais et al., 2015).

Accurate determination of $^{15}\varepsilon_{NAR}$ and $^{15}\varepsilon_{DIN\text{-}R}$ values from the water column is of great importance for quantifying the global N budget, as they dictate the $\delta^{15}N$ of fixed N removed from the marine environment. Further, estimates of the ratio of benthic and water column denitrification occurring globally, or regionally, are dependent upon the $^{15}\varepsilon_{NAR}$ values used (Brandes and Devol, 2002; Sigman et al., 2003; Devries et al., 2012; Somes et al., 2013). Benthic denitrification has an expressed $^{15}\varepsilon_{NAR}$ of approximately 0‰ due to the high extent of N removal in sediments (Brandes and Devol, 1997; Brandes and Devol, 2002; Lehmann et al., 2004; Lehmann et al., 2007). Removal of DIN in sediments without accompanying fractionation dilutes the fractionation associated with water column N loss to achieve isotope balance with $N_2$ fixation, the primary source of new N. Larger water column $^{15}\varepsilon_{NAR}$ values require higher rates of benthic denitrification (Codispoti et al., 2001; Brandes and Devol, 2002), while a lower isotope effect for water column denitrification would require less benthic denitrification (Kritee et al.,

2012; Casciotti et al., 2013; Bourbonnais et al., 2015; Marconi et al., 2017). Whether or not these two scenarios allow a balanced N budget depends greatly on global $N_2$ fixation rates, which are currently poorly constrained (DeVries et al., 2012; Grosskopf et al., 2012; Loescher et al., 2014; Jayakumar et al., 2017). Therefore, uncertainties in marine fixed N loss are directly related to uncertainties in the ratio of benthic to water column denitrification and the corresponding isotope effects for these processes (DeVries et al., 2013; Somes et al., 2013).

In this study, we used concentration and isotope measurements of $NO_2^-$, $NO_3^-$, and $N_2$ from the ETSP ODZ to quantify the amount of fixed N loss using an optimum multiparameter analysis (OMPA) of water mass mixing, and this is used to refine understanding of the expressed isotope effects of ODZ N cycle processes. A series of model experiments was also used to explore the mechanisms responsible for generating variations in the expression of isotope effects under different conditions in the ODZ. These comparisons revealed insights into the cycling and loss of fixed N in the ETSP ODZ.

## Materials and Methods

### *Water mass descriptions*

The samples examined in this study were collected from the ETSP aboard the R/V Nathaniel B. Palmer during austral winter (June-July) 2013. Stations were separated into two sections: 1) a zonal section along 16°S ('Section A'), and 2) a roughly shore-parallel section extending from 12 °S to the northern Chilean coastline at 22 °S ('Section B') (Figure 1).

The water masses that occupy the ODZ ($\sigma_\theta$ = 26.2 to 26.8 kg $m^{-3}$) in this region include Eastern South Pacific Intermediate Water (ESPIW) and Equatorial Subsurface Water (ESSW) (Wyrtki, 1967; Tsuchiya and Talley, 1998; Fiedler and Talley, 2006; Silva et al., 2009; Bostock et al., 2010; Talley et al., 2011). ESPIW is formed by the subduction of relatively cold, fresh water below the warmer, saltier Subtropical Surface Water (STSW) near the coast of Chile (33 to 37°S) creating a distinct shallow salinity minimum (~34) between ~200 and 300 m (Schneider et al., 2003). This water mass is carried towards the equator along the west coast of South America (Reid, 1973) and has been referred to as Subantarctic Water (SAAW) by Silva et al. (2009), Grasse et al. (2012), and Llanillo et al. (2013). Furthermore, Grasse et al. (2013) noted that this water mass has similar properties and formation history to Subantarctic Mode Water (SAMW).

ESSW is a subsurface water type formed near the equator by vertical mixing of waters (Wyrtki, 1967). ESSW occupies the depth range of ~200 m to 600 m, and has higher temperature and salinity than ESPIW (Silva et al., 2009). According to Stramma et al. (2010) and Montes et al. (2010), ESSW is transported eastward into the ODZ by the Equatorial Undercurrent (EUC) and the Southern Subsurface Countercurrent (SSCC). After entering the ODZ, the Peru-Chile Undercurrent (PCUC) and Peru-Chile Countercurrent (PCCC) carry ESSW southward to ~48 °S (Silva and Neshyba, 1979; Tsuchiya and Talley, 1998). ESSW may also be a substantial component of the waters upwelled off the coast of Peru (Kessler, 2006).

*Nutrient concentration and isotopic analyses*

Water samples for nutrient ($NH_4^+$, $NO_2^-$, $NO_3^-$, $PO_4^{3-}$, and silicic acid, $Si(OH)_4$) concentrations, as well as $NO_3^-$ and $NO_2^-$ isotopic analyses, were collected from Niskin bottles on a Seabird CTD-rosette package. Concentrations of $NO_2^-$, $NO_3^-$, $PO_4^{3-}$, and $Si(OH)_4$ were measured on board by a custom nutrient autoanalyzer within 12 h of collection. Nutrients were determined using a combination of analytical components from Alpkem, Perstorp, and Technicon. WOCE-JGOFS standardization and analysis procedures were closely followed as specified by Gordon et al. (1993), including reagent preparation, calibration of labware, preparation of primary and secondary standards, and corrections for blanks and refractive index. $NH_4^+$ was measured using an indophenol blue method modified from Mantoura and Woodward (1983). Dissolved $O_2$ was determined using a Sea-Bird SBE-43 oxygen sensor, calibrated pre-cruise and verified with onboard Winkler titrations (Langdon, 2010) on 53 discrete samples collected during the cruise. The detection limit of the SBE-43 was approximately 1 μM $O_2$.

Seawater samples containing $[NO_2^-] > 0.25$ μM were subsampled on board, and preserved for $NO_2^-$ isotopic analyses. These samples were aliquotted into duplicate 20 mL glass headspace vials, capped with rubber septa, and crimped with aluminum seals. Sealed vials were then purged with $N_2$ gas for 30 minutes to remove dissolved $N_2O$, and treated with a 1:1 mixture of 2M sodium azide and 20% acetic acid to convert $NO_2^-$ to $N_2O$ for isotopic analysis (McIlvin and Altabet, 2005). Triplicate aliquots of isotopic standards RSIL-N23, N7373, and N10219 were also treated with the azide/acetic acid reagent with each batch of samples at sea, and run in parallel with each batch of samples. $\delta^{15}N$ and $\delta^{18}O$ of $NO_2^-$ ($\delta^{15}N_{NO2}$ and $\delta^{18}O_{NO2}$, respectively) were determined by analyzing the $\delta^{15}N$ and $\delta^{18}O$ of the $N_2O$ produced from the azide reaction,

and they are reported in δ notation in per mil (‰) units vs. atmospheric $N_2$ (air) and Vienna Standard Mean Ocean Water (VSMOW), respectively: $\delta^{15}N$ (‰ vs. air) = ($^{15}N/^{14}N \div {}^{15}N/^{14}N_{air}$ - 1) *1000 (‰) and $\delta^{18}O$ (‰ vs. VSMOW) = ($^{18}O/^{16}O \div {}^{18}O/^{16}O_{VSMOW}$ - 1) *1000 (‰). Samples for $\delta^{15}N_{NO2}$ and $\delta^{18}O_{NO2}$ were analyzed in duplicate. Standard deviations for $\delta^{15}N_{NO2}$ and $\delta^{18}O_{NO2}$ were less than 1.5‰ and 1.7‰, respectively.

Seawater samples for $NO_3^-$ isotope analysis were collected in 60 mL syringes and filtered through 0.2 μm Sterivex cartridge filters into 60 mL HDPE Nalgene bottles. Samples were stored frozen on board at −15°C, and remained frozen until samples were transferred to a −20°C laboratory freezer. $\delta^{15}N$ and $\delta^{18}O$ of $NO_3^-$ ($\delta^{15}N_{NO3}$ and $\delta^{18}O_{NO3}$, respectively) were determined by the 'denitrifier method', which relies on the bacterial conversion of $NO_3^-$ to $N_2O$, and subsequent isotopic analysis of the product $N_2O$ (Sigman et al., 2001; Casciotti et al., 2002). Since denitrifying bacteria convert both $NO_3^-$ and $NO_2^-$ to $N_2O$, sulfamic acid was added to samples containing [$NO_2^-$] > 0.2 μM prior to analysis with the denitrifier method (Granger and Sigman, 2009). For those samples, $NO_3^-$ isotope standards USGS32, USGS34, and USGS35 were also treated with sulfamic acid and run in parallel. Otherwise, untreated aliquots of the same standards were used to calibrate $\delta^{15}N_{NO3}$ and $\delta^{18}O_{NO3}$ to air and VSMOW scales (McIlvin and Casciotti, 2011). Analyses were replicated as needed to obtain standard deviations for $\delta^{15}N_{NO3}$ and $\delta^{18}O_{NO3}$ better than 0.2‰ and 0.3‰, respectively.

*$N_2$ concentration and $\delta^{15}N$ analysis*

Duplicate gas samples used for $N_2$:Ar ratios and $\delta^{15}N_{N2}$ were collected in evacuated 185 mL glass flasks sealed with a Louwers-Hapert valve and containing dried mercuric chloride (Emerson et al., 1999). To prevent air contamination when collecting dissolved gas samples, the neck of the closed evacuated glass flask was flushed with $CO_2$ before being flushed with water from the Niskin. Water flowed through tubing directly from the Niskin bottle to the flask without contact with the air and all bubbles were removed from tubing and bottle neck before the valve was opened. After filling a flask to approximately half-full, the valve was closed and the neck was dried and filled with $CO_2$, then capped. In the laboratory, flasks were weighed, and the water was equilibrated with headspace inside the flask by rotating overnight in a water bath at a controlled temperature (~21°C). Water was drained from the flask immediately after removal from the water bath. Gas samples were cryogenically processed to completely remove $CO_2$ and

255 water vapor. At the same time, a known concentration of $^{36}Ar$ spike was added to each sample as
256 done previously in Fuchsman et al. (2008) and Chang et al. (2010, 2012). Samples used for
257 $\delta^{15}N_{N2}$ were also put through an inline CuO furnace to remove all $O_2$. All gas samples were then
258 measured at the Stable Isotope Lab, School of Oceanography, University of Washington on a
259 Finnigan Delta XL isotope ratio mass spectrometer against an air standard that had been heated
260 in the inline CuO furnace to remove $O_2$.
261
262 *Calculating the concentration and $\delta^{15}N$ of biogenic $N_2$*
263 Biogenic $N_2$ concentrations were determined by subtracting background $N_2$ ($[N_2]_{back}$)
264 from our measured $N_2$ concentrations ($[N_2]_{obs}$):
265
266 $$[N_2]_{bio} = [N_2]_{obs} - [N_2]_{back} \quad (4)$$
267
268 Background measurements from oxic waters ventilating the ETSP (Chang et al., 2010) contain
269 $N_2$ originally from equilibrium with air, but mixing of water masses causes gases to become
270 supersaturated in the ocean (Henning et al., 2006; Ito et al., 2007). Thus, unless all the end
271 members are clearly known, as can be true in simple systems (Fuchsman et al., 2008; Manning et
272 al., 2010), it is best to empirically determine the background concentrations (Chang et al., 2010,
273 2012). Here, we used the data from Chang et al. (2010) to determine the background $N_2$ for our
274 $[N_2]_{bio}$ calculations (eq. 4).
275 In order to calculate the $\delta^{15}N$ of biogenic $N_2$ ($\delta^{15}N_{N2,bio}$), we extend the mass balance
276 considerations described above to its isotopic composition:
277
278 $$\delta^{15}N_{N2,bio}*[N_2]_{bio} = \delta^{15}N_{N2,obs}*[N_2]_{obs} - \delta^{15}N_{N2,back}*[N_2]_{back} \quad (5)$$
279
280 where the concentrations of each pool are indicated with square brackets and the isotopic
281 composition with '$\delta^{15}N_{N2}$' with the corresponding subscript. It was assumed that background
282 $\delta^{15}N_{N2}$ in waters outside the ETSP ODZ is roughly that expected at equilibrium based on
283 observed temperature and salinity (0.68 to 0.72‰; Klots and Benson, 1963; Knox et al., 1992).
284 We use 0.7‰ as the base value for $\delta^{15}N_{N2,back}$ in these calculations, but evaluate the sensitivity of

this assumption by calculating the $\delta^{15}N_{N2,bio}$ values using a range of $\delta^{15}N_{N2,back}$ values between 0.68‰ and 0.72‰.

*Optimum Multiparameter Analysis*

Optimum multiparameter analysis (OMPA) was performed on all samples within the density range $\sigma_\theta$ = 26.0 – 27.0 kg m$^{-3}$, containing the ETSP ODZ ($\sigma_\theta$ = 26.2 - 26.8 kg m$^{-3}$). The OMPA method relies on a set of linear mixing equations to solve for the fractions of the chosen water types, $x_i$ (Mackas et al., 1987; Tomczak and Large, 1989), which can be solved using a non-negative least squares method (we use the 'nonneglsq' function included in the MATLAB Optimization Toolbox):

$$x_{ESSW} * T_{ESSW} + x_{ESPIW} * T_{ESPIW} = T_{obs} + T_R \quad (6A)$$

$$x_{ESSW} * S_{ESSW} + x_{ESPIW} * S_{ESPIW} = S_{obs} + S_R \quad (6B)$$

$$x_{ESSW} + x_{ESPIW} = 1 + x_R \quad (6C)$$

based on the temperature (T) and salinity (S) of the water types ESSW and ESPIW. The subscript 'R' indicates the residual term for each parameter ($T_R$ being the residual in temperature, $S_R$ being the residual in salinity, and $x_R$ being the residual in the water mass fraction). Residuals in equations 6A-C result when the optimal solution for $x_{ESSW}$ and $x_{ESPIW}$ does not exactly match the observed T or S, or does not sum exactly to 1. We note that only two equations are needed to perform the OMPA, since only two water masses are under consideration (ESSW and ESPIW). However, the third equation (mass conservation) provides an over determination of the system, allowing estimation of the error associated with water type selections. The weighting of parameters is determined by taking the ratio of: a) the range of a given property to b) the uncertainty of the measurement (Glover et al., 2011). The weights used were 140, 100, and 140 for T, S, and mass conservation, respectively.

In order to determine the T and S end member values for ESSW and ESPIW, we used the 'thermocline array' approach described by Jenkins et al (2015). First, geographic ranges were defined for characterization of ESSW (5°N to 5°S and 80°W to 90°W) and ESPIW (20°S to 30°S and 80°W to 90°W). Next, all T and S values were obtained from World Ocean Atlas 2013 (WOA13) within the defined density range ($\sigma_\theta$ = 26.0 to 27.0 kg m$^{-3}$) and interpolated to density

316 in increments of 0.01 kg $m^{-3}$ (Figure S1A and B). This method for determining water mass
317 fractions at small density increments has the benefit of ensuring that mixing of water masses in
318 the OMPA is primarily along isopycnal surfaces. Water mass analysis was then performed on
319 each individual water sample contained within the prescribed density range by matching the
320 sample density to the nearest increment of water mass density, and then taking the T and S
321 values of ESSW and ESPIW at that density (Jenkins et al., 2015; Peters et al., 2017). Fractions of
322 ESSW and ESPIW in a given sample were then determined from equations 6A-C.
323
324 *Estimating DIN deficit from OMPA*
325 In this study, we used the OMPA results to provide an alternative estimate of the DIN
326 deficit ($[DIN]_{def,OMP}$), which might better reflect the local biogeochemistry (Mackas et al., 1987;
327 Tomczak and Large, 1989). OMPA allows for determination of the background $[O_2]$ ($[O_2]_{back}$)
328 that results from mixing the $O_2$ concentrations of the two source water masses (ESSW and
329 ESPIW) in their prescribed fractions for each sample:
330
331 $$[O_2]_{back} = x_{ESPIW} * [O_2]_{ESPIW} + x_{ESSW} * [O_2]_{ESSW} \quad (7)$$
332
333 End member values of $[O_2]$ for ESSW and ESPIW required for the $[O_2]_{back}$ calculation
334 were interpolated onto the same density grid as T and S (described above) from WOA13 annual
335 average data. The background $[O_2]$ can be used to calculate the amount of $O_2$ respired between
336 the source waters and the water sample. This is analogous to the 'True Oxygen Utilization'
337 (TOU) described by Broecker and Peng (1982):
338
339 $$TOU = [O_2]_{back} - [O_2]_{obs} \quad (8)$$
340
341 Where $[O_2]_{obs}$ is the measured $[O_2]$ in a given sample. The TOU can then be used to estimate the
342 quantity of $NO_3^-$ added by remineralization ($[NO_3^-]_{remin}$) by making an assumption about the
343 stoichiometry of $NO_3^-$ produced relative to $O_2$ respired ($\Delta NO_3^-/\Delta O_2$):
344
345 $$[NO_3^-]_{remin} = TOU * \Delta NO_3^-/\Delta O_2 \quad (9)$$
346

Global averages of $\Delta NO_3^-/\Delta O_2$ range between 16/180 (Anderson and Sarmiento, 1994) and 16/150 (Anderson, 1995). We adopted a standard value of $\Delta NO_3^-/\Delta O_2 = 16/150$, but tested the sensitivity of this assumption (Figure S2).

Using the water type fractions from the OMPA output and the associated $[NO_3^-]$ of each water type at the sample density (interpolated from WOA13), background $NO_3^-$ ($[NO_3^-]_{back}$) was also calculated for each sample by summing the contributions from each water type :

$$[NO_3^-]_{back} = x_{ESPIW} * [NO_3^-]_{ESPIW} + x_{ESSW} * [NO_3^-]_{ESSW} \quad (10)$$

where '$x_i$' and $[NO_3^-]_i$ represent the fractional contribution and $NO_3^-$ concentration of each water type indicated by the subscripts. Next, the expected DIN from OMPA ($[DIN]_{exp,OMP}$) was determined by adding the remineralized $NO_3^-$ to background $NO_3^-$:

$$[DIN]_{exp,OMP} = [NO_3^-]_{remin} + [NO_3^-]_{back} \quad (11)$$

Finally, a new estimate of the DIN deficit from OMPA ($[DIN]_{def,OMP}$) could be calculated:

$$[DIN]_{def,OMP} = [DIN]_{exp,OMP} - [DIN]_{obs} \quad (12)$$

This approach yields alternative estimates of fixed N loss in regions where $[PO_4^{3-}]$ data are not available, or where not all of the measured $[PO_4^{3-}]$ is associated with remineralization of N. Further, it relies on estimation of $O_2$ consumption along fine-scale density increments. This is important because the ETSP ODZ lies in a 'shadow' zone where ventilation occurs along isopcynals, rather than diapycnally (Luyten et al., 1983; Gehrie et al., 2006). Moreover, it has been demonstrated that calculations of apparent oxygen utilization (AOU), which assumes the background $[O_2]$ is at equilibrium with the atmosphere, may overestimate respiration (Ito et al., 2004).

## Results

*Nitrite, oxygen, and $[DIN]_{def,P}$ sections*

Concentrations of dissolved $O_2$ ranged from near saturation at the sea surface to less than 5 μM in the core of the ODZ at most stations (Figure 2A, B). Section A showed an east-west gradient in dissolved $O_2$ in the ODZ, with lower concentrations at the eastern end of the section and higher $O_2$ concentrations in the western end (Figure 2A). In section B, low [$O_2$] was observed throughout the ODZ, leading to less of an $O_2$ gradient within the ODZ, although the thickness of the low $O_2$ layer varied with latitude (Figure 2B).

Subsurface [$NO_2^-$] was elevated (> 6 μM) in the ODZ at the eastern-most stations along section A (Figure 2C), but lower at the stations to the west. This feature, known as the secondary $NO_2^-$ maximum (SNM), coincided with the lowest dissolved [$O_2$] (Figure 2A). The highest subsurface accumulations of $NO_2^-$ were observed in section B at stations near the Chilean coast (stations BB2, 21, and 22), and farther north along the same section (stations 5, 7, and 9). $NO_2^-$ was undetectable at station 8, the northernmost station of the coastal section, as well as the stations near the southern end of the section (stations 1, 19, and 20). This is consistent with the slightly higher concentrations of dissolved $O_2$ observed at these stations (~8 to 10 μM; Figure 2B), and suggests that these stations with an absence of subsurface $NO_2^-$ may not be functionally anoxic (Thamdrup et al., 2012).

While [$NO_2^-$] peaked in the core of the ODZ, the $[DIN]_{def,P}$ (eq. 3) was generally highest at the top of the ODZ ($\sigma_\theta$ = 26.2 kg $m^{-3}$) and decreased toward the bottom of the ODZ in both sections (Figures 2E and 2F). $[DIN]_{def,P}$ along section A was higher at the eastern end of the section (up to 25 μM) and decreased toward the western end of the section, except for the elevated $[DIN]_{def,P}$ at station 11 (Figure 2E), which also contained lower dissolved $O_2$ (Figure 2A) and elevated $NO_2^-$ concentrations (Figure 2C). $[DIN]_{def,P}$ values were highest at the near-shore stations in section B, reaching values of ~30 to 35 μM at the top of the ODZ (Figure 2F). $[DIN]_{def,P}$ values were not as high at stations 1 and 19, reaching values of only 18 μM. $[DIN]_{def,P}$ generally increased again (~20 μM ) at the stations farther north along the section, which contained lower $O_2$ (Figure 2B) and elevated $NO_2^-$ concentrations (Figure 2D). $[DIN]_{def,P}$ values were lowest at station 8, reaching only ~ 11 μM. The [$NO_3^-$] and [$PO_4^{3-}$] measurements that were used to calculate $[DIN]_{def,P}$ are shown in Figure S3.

*OMPA results*

The spread of T and S along isopycnals in the samples from this study illustrates the mixing between ESSW and EPISW within the ODZ ($\sigma_\theta$ = 26.0 - 27.0 kg $m^{-3}$) (Figure S1). The percentage of ESSW increased from the top of the ODZ (40-60%) toward the middle of the ODZ, reaching maxima near 80-100% between $\sigma_\theta$ = 26.5 and 26.6 kg $m^{-3}$ (Figure S4A). ESSW then decreased to 60-80% toward the bottom of the ODZ. ESSW percentages were greatest at the northern-most station along the coastal section (station 8) and generally decreased at stations farther south along the coastal section. This trend might be expected, since ESSW is defined in the equatorial region, and thus contributions of ESSW should decrease away from the equator as it mixes with the southern end member (ESPIW). However, an apparent increase in ESSW was observed at BB2, the station nearest the Peruvian coast. This is consistent with previous studies that proposed that both the EUC and SSCC are important sources of upwelled water along the coastal region of the ETSP (Kessler, 2006; Stramma et al., 2010; Montes et al., 2010). The percentage of ESPIW contribution to the samples showed a mirror image of ESSW (Figure S4B), as only two water masses were used in the OMPA. The maximum percentage of ESPIW (80%) was observed at stations 14 and 19. In the core of the ODZ, ESPIW generally ranged from 0-20%, although it contributed up to 40-60% at station 19. ESPIW appeared to have a stronger influence at the stations with higher [$O_2$], lower [$NO_2^-$], and less fixed N loss.

Due to the strong influence of ESSW in the ODZ, the background [$NO_3^-$], [$PO_4^{3-}$], and [$O_2$] calculated from the OMPA were similar to the ESSW end member values (Figure 3). $[O_2]_{back}$ ranged between 100 and 150 μM at $\sigma_\theta$ = 26.0 kg $m^{-3}$, and reached minima of 30 μM to 50 μM at $\sigma_\theta$ = 26.6 kg $m^{-3}$ (Figure 3A). $[O_2]_{back}$ gradually increased between $\sigma_\theta$ = 26.6 - 27.0 kg $m^{-3}$ marking the greater influence of ESPIW in the lower ODZ. Observed [$O_2$] was considerably lower than $[O_2]_{back}$, illustrating the effect of $O_2$ respiration. It was generally < 50 μM between $\sigma_\theta$ = 26.0 - 27.0 kg $m^{-3}$ and below 2 μM between 26.2 - 26.8 kg $m^{-3}$.

Background [$NO_3^-$] was ~20 μM at $\sigma_\theta$ = 26.0 kg $m^{-3}$ and increased gradually to 30 μM at $\sigma_\theta$ = 26.6 kg $m^{-3}$ (Figure 3B), while observed [$NO_3^-$] showed a distinct minimum in this density range, reflecting DIN loss in the ODZ. Background [$PO_4^{3-}$] increased from ~1.5 μM to 2.5 μM across the same density range (Figure 3C), while observed [$PO_4^{3-}$] ranged up to 2.7 μM at the top of the ODZ, reflecting inputs of $PO_4^{3-}$ to the water column. The $[DIN]_{exp,P}$ likewise peaked at the top of the ODZ (Figure 3D), as this is derived directly from observed [$PO_4^{3-}$].

Concentrations of remineralized $NO_3^-$ were highest in the oxycline above the ODZ (up to 10 μM), and decreased to 5 μM toward the bottom of the ODZ (Figure 3D), as might be expected from decreasing particulate flux with depth. Adding $[NO_3^-]_{remin}$ to $[NO_3^-]_{back}$ yields the $[DIN]_{exp,OMP}$, which increased gradually with depth through the ODZ, rather than showing a peak at the top of the ODZ (Figure 3D). Indeed, the $[DIN]_{exp,OMP}$ values were always lower than $[DIN]_{exp,P}$ in the ODZ, with the largest difference occurring at $\sigma_\theta$ = 26.2 - 26.4 kg $m^{-3}$. These results show significant differences in DIN deficit estimates using different assumptions.

*Comparison of $[N_2]_{bio}$ and DIN deficit*

$N_2$:Ar measurements allowed estimates of biologically produced $N_2$ ($[N_2]_{bio}$) at select stations (Figure 4). At each of these stations, a maximum in $[N_2]_{bio}$ was observed at the top of the ODZ near the base of the upper oxycline, with the highest $[N_2]_{bio}$ found at station BB2 (31 μM). Station 8 had the lowest $[N_2]_{bio}$, with a maximum reaching only 18 μM. $[DIN]_{def,P}$ agreed well with $[N_2]_{bio}$ in both magnitude and shape in the upper and middle part of the ODZ ($\sigma_\theta$ = 26.2 - 26.6 kg $m^{-3}$), but appeared to diverge from $[N_2]_{bio}$ in the bottom of the ODZ at most stations ($\sigma_\theta$ = 26.6 - 27.0 kg $m^{-3}$; Figure 4). The profiles of $[DIN]_{def,OMP}$ appeared to better match the overall shape of the $[N_2]_{bio}$ profiles, but were lower than $[N_2]_{bio}$ by ~5 μM throughout (Figure 4). Thus, inconsistencies between the measured $[N_2]_{bio}$ values and estimates of fixed N loss from $[PO_4^{3-}]$ and OMPA need to be addressed.

A regression of $[N_2]_{bio}$ versus the $[DIN]_{def,P}$ (Figure 5, open symbols) yielded a slope of 0.75 ± 0.05 (± 0.1 at the 95% confidence level), suggesting that $[DIN]_{def,P}$ overestimates the biological production of $[N_2]$ by 25%. However, the slope of $[N_2]_{bio}$ versus $[DIN]_{def,OMP}$ (Figure 5, filled symbols) had a slope of 1.01 ± 0.06 (± 0.13 at the 95% confidence level), suggesting that $[DIN]_{def,OMP}$ more closely predicts the variation in biological production of $[N_2]$. However, both methods for calculating the DIN deficit yielded a substantial y-intercept (Figure 5A), which indicates the source waters for this region of the ETSP may have pre-existing $[N_2]_{bio}$ ranging from 5.3 to 6.3 μM that is not accounted for in the background $[N_2]$ calculation. In contrast, the DIN deficit present in source waters is accounted for in $[DIN]_{def,P}$ and $[DIN]_{def,OMP}$. This explanation of the non-zero intercept of $[N_2]_{bio}$ is supported by results from Bourbonnais et al. (2015), who reported $[N_2]_{bio}$ ranging from 4-8 μM between $\sigma_\theta$ = 26.0 - 27.0 kg $m^{-3}$ at a station

(1.67°N, 85.83°W) within the geographic range of our ESSW end-member definition. If we assume the density-dependent $[N_2]_{bio}$ reported by Bourbonnais et al. (2015) represents the pre-existing $[N_2]_{bio}$ in our region, we can subtract this from the measured $[N_2]_{bio}$ in each of our samples to obtain the $[N_2]_{bio}$ signal generated locally ($[N_2]_{bio,local}$). We found that $[N_2]_{bio,local}$ agreed well with $[DIN]_{def,P}$ in the upper ODZ ($\sigma_\theta$ = 26.2 - 26.4 kg $m^{-3}$), while $[DIN]_{def,P}$ generally exceeded $[N_2]_{bio,local}$ below $\sigma_\theta$ = 26.4 kg $m^{-3}$ (Figure 4). On the other hand, we found that $[N_2]_{bio,local}$ and $[DIN]_{def,OMP}$ were nearly indistinguishable below $\sigma_\theta$ = 26.4 kg $m^{-3}$, and that $[N_2]_{bio,local}$ exceeded $[DIN]_{def,OMP}$ by as much as 7 μM at the peak in $[N_2]_{bio,local}$ between $\sigma_\theta$ = 26.2 - 26.4 kg $m^{-3}$ (Figure 4). Regressing $[N_2]_{bio,local}$ against $[DIN]_{def,P}$, a slope of 0.83 ± 0.06 was obtained (± 0.11 at the 95% confidence level; dashed line in Figure 5B). On the other hand, the regression of $[N_2]_{bio,local}$ vs. $[DIN]_{def,OMP}$ revealed a slope of 1.13 ± 0.07 (± 0.14 at the 95% confidence level; black line in Figure 5B). These slopes were relatively insensitive to the N:P or $\Delta NO_3^-/\Delta O_2$ values used to calculate $[DIN]_{def,P}$ or $[DIN]_{def,OMP}$, respectively (Figure S2). The mechanisms that could drive variations in the relationship between $[N_2]_{bio,local}$ and DIN deficit estimates are discussed below.

*Isotopic measurements of $NO_2^-$, $NO_3^-$ and $N_2$*

Elevations in $\delta^{15}N_{NO3}$ and $\delta^{18}O_{NO3}$ were found in the ODZ at all stations, with the highest $\delta^{15}N_{NO3}$ (30‰) and $\delta^{18}O_{NO3}$ (26‰) values occurring at the stations nearest to shore (stations BB2, 21, and 22; Figure 6). Most of the stations demonstrated maxima in $\delta^{15}N_{NO3}$ (Figure 6A and B) and $\delta^{18}O_{NO3}$ (Figure 6C and D) near the top of the ODZ, but they remained elevated throughout the ODZ. The maxima in $\delta^{15}N_{NO3}$ and $\delta^{18}O_{NO3}$ were the least pronounced at stations 8 and 19, where no SNM was observed. The overall trends in $\delta^{15}N_{NO3}$ and $\delta^{18}O_{NO3}$ appeared to match those of $[DIN]_{def,P}$ (Figures 2E and F), consistent with dissimilatory $NO_3^-$ reduction contributing to the elevated $\delta^{15}N_{NO3}$ and $\delta^{18}O_{NO3}$ values in the ODZ.

Additional insights are provided by comparing $\delta^{15}N_{NO3}$ with measurements of $\delta^{15}N_{NO2}$ and $\delta^{15}N_{N2,bio}$ (Figure 7). $\delta^{15}N_{NO2}$ ranged between -8 and -20‰ at the top of the ODZ, and decreased gradually to values as low as -38‰ at the bottom of the ODZ. Where $NO_2^-$ was present in the water above the ODZ, a feature known as the primary $NO_2^-$ maximum (PNM), $\delta^{15}N_{NO2}$ was closer to 0‰ (e.g., Figure 7D). $NO_2^-$ was depleted in $^{15}N$ relative to $NO_3^-$ by 10‰ to

40‰ in the ODZ, with the offset generally smallest near the top of the ODZ and increasing with depth.

At the stations where an SNM was present (9, 17, 18, BB2), $\delta^{15}N_{N2,bio}$ also decreased from -10‰ at the top of the ODZ to -40‰ towards the bottom, closely tracking the observed $\delta^{15}N_{NO2}$ (Figure 7). Beneath the SNM, $\delta^{15}N_{N2,bio}$ returned to higher values, similar to those observed above the SNM. At stations 8 and 19, no SNM was observed, but the presence of biogenic [$N_2$] permitted $\delta^{15}N_{N2,bio}$ measurements (Figure 7A and E, respectively). At these stations, the $\delta^{15}N_{N2,bio}$ values showed maximal values (−16‰ to −13‰) near the top of the ODZ (~200 m at both stations) where the $[N_2]_{bio}$ maxima occurred. At both stations, $\delta^{15}N_{N2,bio}$ decreased within the middle of the ODZ (to values of −35‰ and −31‰, respectively), before increasing again at the bottom of the ODZ. The lack of $NO_2^-$ suggests that these stations were not functionally anoxic (Thamdrup et al., 2012), although other geochemical signals of N loss were present: elevated $\delta^{15}N_{NO3}$, accumulation of biogenic $N_2$, and a DIN deficit. Possible explanations for the observed trends in $\delta^{15}N_{N2,bio}$ and $\delta^{15}N_{NO2}$ are discussed below.

*Isotope effect estimates from closed system Raleigh model*

Together with the estimates of DIN deficit, the $\delta^{15}N_{NO3}$, $\delta^{15}N_{NO2}$, and $\delta^{15}N_{N2,bio}$ could be used to estimate the isotope effects for N loss in the ETSP ODZ. These are important for constraining the marine nitrogen budget by isotope mass balance. The isotope effects for $NO_3^-$ reduction ($^{15}\varepsilon_{NAR}$ and $^{18}\varepsilon_{NAR}$) and total DIN ($NO_3^-$ + $NO_2^-$) removal ($^{15}\varepsilon_{DIN\text{-}R}$) were estimated using the closed system Rayleigh equations:

$$\delta_s = \delta_{s,0} - \varepsilon * \ln(f) \quad (14)$$

$$\delta_{pa} = \delta_{s,0} + \varepsilon * f * \ln(f)/(1-f) \quad (15)$$

Where $\delta_s$ is the measured isotopic composition of the substrate ($NO_3^-$ or DIN), $\delta_{pa}$ is the isotopic composition of the accumulated product (biogenic $N_2$), $\delta_{s,0}$ is the initial isotopic composition of the substrate ($NO_3^-$ or DIN), and $\varepsilon$ is the isotope effect for the reaction ($NO_3^-$ reduction or DIN removal). For $^{15}\varepsilon_{NAR}$ and $^{18}\varepsilon_{NAR}$, the fraction of initial $NO_3^-$ remaining ($f$) was calculated from $[NO_3^-]_{obs}/[NO_3^-]_{initial}$; for $^{15}\varepsilon_{DIN\text{-}R}$, $f$ was calculated from $[DIN]_{obs}/[NO_3^-]_{initial}$. From equation 14,

each isotope effect was taken from the slope of -ln($f$) versus the isotopic composition ($\delta^{15}N$ or $\delta^{18}O$) of the substrate ($NO_3^-$ or DIN). From equation 15, the isotope effect was taken from the slope of $f$*ln($f$)/(1-$f$) vs. the $\delta^{15}N$ of biogenic $N_2$.

The isotope effects were first estimated by combining data from the ODZ across all stations, using three different approaches for estimating the initial $NO_3^-$. The 'sum of N pools' used observed $NO_3^-$, $NO_2^-$, and biogenic $N_2$ to estimate the initial [$NO_3^-$]. This approach inherently includes aerobic remineralization that occurs along the flow path, and the organic N contribution to $[N_2]_{bio}$ from anammox in the ODZ. Because of this inclusion of ammonium from organic N degradation, the sum of N pools may overestimate initial [$NO_3^-$], but correctly estimate initial dissolved inorganic N. The $[DIN]_{exp,P}$ approach used equation 1 and accounts for aerobic remineralization that occurs along isopycnals. It should also include anaerobic respiration of organic matter and the contribution from anammox, making it similar to the sum of N pools approach, except where sediments release $PO_4^{3-}$ to the overlying waters. The $[DIN]_{exp,OMP}$ approach used the OMP analysis to estimate the initial [$NO_3^-$] (equation 11), and includes aerobic remineralization but not anaerobic respiration of organic matter. This method of calculating $f$ should thus give the lowest initial [$NO_3^-$], thus the highest $f$ values and the highest isotope effects for a given amount of DIN consumption.

When plotting all of the ODZ data together, the estimates for the N isotope effect for $NO_3^-$ reduction ($^{15}\varepsilon_{NAR}$) ranged from 16.5 to 19.6‰, depending on the method of calculating $f$ (Figure S5A, B, C). These $^{15}\varepsilon_{NAR}$ values were similar, though slightly lower than those obtained by Bourbonnais et al. (2015) from two coastal eddies in the ETSP (~19.5‰ to 20.9‰), and lower than that estimated by a modeling study conducted using high resolution $NO_3^-$ and $NO_2^-$ isotope data from this same cruise (18 to 23‰; Peters et al., 2016). Estimates of the O isotope effect for $NO_3^-$ reduction ($^{18}\varepsilon_{NAR}$) were slightly lower, ranging from 14.7 to 17.6‰ (Figure S5D, E, F). The apparent isotope effects for DIN removal ($^{15}\varepsilon_{DIN\text{-}R}$) were lower still, ranging from 10.9‰ to 13.7‰ (Figure S5G, H, I). These estimates were also similar to those obtained by Bourbonnais et al. (2015) (12.6 to 13.2‰). In these estimates, the isotope effects using the 'sum of N pools' and $[DIN]_{exp,P}$ approaches were indistinguishable, while the $[DIN]_{exp,OMP}$ approach yielded slightly higher isotope effects (Figure S5). The $^{15}\varepsilon_{DIN\text{-}R}$ estimate obtained using all of the $\delta^{15}N_{N2,bio}$ data in equation 15 ranged from 32-34 ± 8-10‰, depending on the method of calculating $f$ (Figure S6). This is generally higher than the $^{15}\varepsilon_{DIN\text{-}R}$ estimated from $\delta^{15}N_{DIN}$, but

the poor $r^2$ and high uncertainty in both the $\delta^{15}N_{2,bio}$ measurements and the fit leaves a wide range of possible solutions.

In comparison to earlier studies (Bourbonnais et al., 2015; Fuchsman et al., 2017), we also noted that the data from different density layers showed different trajectories in the Rayleigh plots, with the deeper isopycnal layers showing a slightly higher slope (Figure S5). In order to assess the apparent variation of isotope effects with depth, the data were subdivided into 0.1 kg $m^{-3}$ density intervals. Calculation of $^{15}\varepsilon_{NAR}$, $^{18}\varepsilon_{NAR}$, and $^{15}\varepsilon_{DIN\text{-}R}$ values across these smaller density intervals confirmed significant variations with depth through the ODZ, regardless of method of determining *f* (Table 1). Using the sum of N pools to calculate *f*, $^{15}\varepsilon_{NAR}$ increased from 17.7 ± 2.0‰ (± 5.1‰ at the 95% confidence level) in the shallowest ODZ ($\sigma_\theta$ = 26.2 - 26.3 kg $m^{-3}$) to 34.6 ± 2.9‰ (± 6.6‰ at the 95% confidence level) in the middle ODZ ($\sigma_\theta$ = 26.5 - 26.6 kg $m^{-3}$), before dropping to 30.5 ± 1.1‰ at $\sigma_\theta$ = 26.7 - 26.8 kg $m^{-3}$ (Table 1). Using $[DIN]_{exp,P}$ and $[DIN]_{exp,OMP}$, $^{15}\varepsilon_{NAR}$ values increased steadily from the top of the ODZ to maxima of 29.3 ± 2.4‰ (± 7.6‰ at the 95% confidence level) and 34.4 ± 8.4‰ (± 26.7‰ at the 95% confidence level), respectively, at the bottom of the ODZ (Table 1).

$^{18}\varepsilon_{NAR}$ values also generally increased with density (Table 1). Furthermore, with the exception of the bottom density interval ($\sigma_\theta$ = 26.7 - 26.8 kg $m^{-3}$), where limited data and poor $r^2$ values likely biased the isotope effect estimates, the $^{18}\varepsilon_{NAR}$ values at a given density interval were less than the $^{15}\varepsilon_{NAR}$ values at the same density. $NO_3^-$ reduction during denitrification is expected to fractionate N and O isotopes in $NO_3^-$ equally (Granger et al., 2008; Krittee et al., 2012; Triebergs et al., 2014), although mismatches between $^{18}\varepsilon_{NAR}$ and $^{15}\varepsilon_{NAR}$ observed in other ODZ studies have been interpreted to reflect the processes of $NO_2^-$ oxidation acting upon the N and O isotopes of $NO_3^-$ in ODZs (Sigman et al., 2005; Casciotti et al., 2013; Casciotti, 2016; Bourbonnais et al., 2015).

$^{15}\varepsilon_{DIN\text{-}R}$ values showed greater variation across the density intervals and generally showed the lowest values in the upper portion of the ODZ (8-19‰; Table 1). Here, the $^{15}\varepsilon_{DIN\text{-}R}$ values were significantly lower than $^{15}\varepsilon_{NAR}$ values ($p < 0.0001$). Most notable were the low apparent $^{15}\varepsilon_{DIN\text{-}R}$ values at $\sigma_\theta$ 26.4-26.5 kg $m^{-3}$, in the upper portion of the SNM. $^{15}\varepsilon_{DIN\text{-}R}$ values between 26.5 and 26.7 kg $m^{-3}$ (31-36‰) were not significantly different from $^{15}\varepsilon_{NAR}$ values (33-35‰). Low numbers of observations and low $r^2$ give the $^{15}\varepsilon_{DIN\text{-}R}$ values at the bottom of the ODZ ($\sigma_\theta$ =

588 26.7 - 26.8 kg $m^{-3}$) a high degree of uncertainty. Overall, the calculation of $^{15}\varepsilon_{DIN\text{-}R}$ from
589 $[DIN]_{exp,OMP}$ appeared to be similar to those obtained from the sum of the N pools and $[DIN]_{exp,P}$,
590 and any differences were not statistically significant (Table 1).
591
592 **Discussion**
593 *Comparison of $[N_2]_{bio}$ with $[DIN]_{def,P}$ and $[DIN]_{def,OMP}$*
594 Previous studies have compared $[N_2]_{bio}$ and $[DIN]_{def,P}$ measurements from ODZs, and
595 have remarked on general similarities between the two (Chang et al., 2010; Chang et al., 2012;
596 Bourbonnais et al., 2015). In this study, there were significant differences between these
597 estimates of fixed N loss, along with the $[DIN]_{def}$ estimated with the OMP analysis. Because of
598 the fact that different assumptions are used in calculating $[DIN]_{def,P}$ and $[DIN]_{def,OMP}$, we found
599 the examination of the relationship between them and $[N_2]_{bio}$ instructive as to the local
600 biogeochemistry and the mechanisms of fixed N loss. A slope less than 1 observed in the
601 regression of $[N_2]_{bio,local}$ vs. $[DIN]_{def,P}$ (Figure 5B) could arise through loss of biogenic $N_2$ by gas
602 exchange, or release of $PO_4^{3-}$ from sediments not linked to $NO_3^-$ regeneration. The first scenario
603 would imply that $[N_2]_{bio,local}$ is underestimated, while the second scenario would suggest that
604 $[DIN]_{def,P}$ overestimates the DIN deficit. Gas exchange occurring at the top of the ODZ is
605 plausible where isopycnals tilt upwards towards the coast. However, omitting data from the most
606 coastal station (BB2) and from all stations above $\sigma_\theta$ = 26.4 kg $m^{-3}$ did not have a significant
607 impact on the slope of $[N_2]_{bio,local}$ vs. $[DIN]_{def,P}$ (Supplementary Material; Figure S7).
608 In contrast, release of $PO_4^{3-}$ to the water column from sediments was recently found in
609 the coastal ETSP (Hu et al., 2016). In order to explore the influence of sediment $PO_4^{3-}$ release on
610 $[DIN]_{def,P}$ at our stations, we estimated the concentration of 'excess' $[PO_4^{3-}]$ (referred to as $[PO_4^{3-}]_{xs}$), which represents $PO_4^{3-}$ not associated with aerobic respiration. This corresponds to $PO_4^{3-}$
612 regenerated anaerobically ($[PO_4^{3-}]_{xs,anox}$), plus that released from sediments ($[PO_4^{3-}]_{xs,sed}$). If no
613 $[PO_4^{3-}]$ is released from sediments, this measure should correspond stoichiometrically with $NH_4^+$
614 released from anaerobic heterotrophic respiration and converted to $N_2$ via anammox. In the case
615 that $PO_4^{3-}$ is released from sediments, the extra $[PO_4^{3-}]_{xs}$ above that required to match the $[N_2]_{bio}$
616 signature would correspond to that derived from sediments (Supplementary Material).
617 Our simple calculations suggested that approximately 50% of $[PO_4^{3-}]_{xs}$ derives from
618 anoxic remineralization and about 50% from sediments (Figure S8). This contribution from

sediments would be lower if anammox contributed more than 29% of the $N_2$ production. While our comparison of $[N_2]_{bio,local}$ to $[DIN]_{def,OMP}$ suggests that this is a reasonable overall estimate (see below), a study from this same cruise to the ETSP demonstrated that anammox can contribute more than 29% of the total N loss if $NO_2^-$ oxidation is an important sink of $NO_2^-$ (Peters et al., 2016; Babbin et al., 2017). Anammox may also exceed 29% of $[N_2]_{bio}$ if dissimilatory $NO_3^-$ reduction to ammonium ('DNRA') is important (Lam et al., 2009). However, our results suggest that anammox contributes approximately 29% of $[N_2]_{bio}$ (see below) and indicate that caution should be taken when using $[PO_4^{3-}]$ measurements to estimate fixed N loss in ODZs when sediment influence is important. If $[PO_4^{3-}]_{xs}$ causes $[DIN]_{def,P}$ estimates to overestimate N loss, then $[DIN]_{def,OMP}$, which does not rely on $[PO_4^{3-}]$ measurements, may provide a better estimate.

$[DIN]_{def,OMP}$ appeared to match $[N_2]_{bio,local}$ best in the lower ODZ, and it underestimated $[N_2]_{bio,local}$ in the upper ODZ, especially at the peak in $[N_2]_{bio,local}$ (Figure 4). One way $[DIN]_{def,OMP}$ could underestimate $[N_2]_{bio,local}$ is if $NH_4^+$ released from organic matter contributed to $N_2$ production via anammox. Since a portion of the biogenic $N_2$ produced by anammox derives from $NH_4^+$ released from anaerobic remineralization of organic matter (i.e., dissimilatory $NO_3^-$ reduction and heterotrophic denitrification) along with a stoichiometric amount of P, the $[DIN]_{def,P}$ would capture this N removal from the organic N pool, while the $[DIN]_{def,OMP}$ estimate would not. $NH_4^+$ was below detection in the ODZ during this cruise (Peng et al., 2016; Babbin et al., 2017), and therefore did not contribute to the observed DIN pool. One potential fate for $NH_4^+$ released during heterotrophic $NO_3^-$ and $NO_2^-$ reduction is oxidation to $NO_2^-$, but ammonia oxidation rate measurements from this cruise indicated that $NH_4^+$ oxidation rates in this part of the water column were below detection (Peng et al., 2016). Thus, anammox is the best explanation for the removal of $NH_4^+$ and the observed decoupling of $[N_2]_{bio,local}$ and $[DIN]_{def,OMP}$. Indeed, anammox rates are often maximal at the top of the ODZ (Dalsgaard et al., 2012; Babbin et al., 2017), where the greatest discrepancies between $[DIN]_{def,OMP}$ and $[N_2]_{bio,local}$ were found.

Here, the slope of 1.17 of $[N_2]_{bio,local}$ vs. $[DIN]_{def,OMP}$ (Figure 5B) suggests that for every 1.17 moles of biogenic $N_2$ produced, 0.17 moles derive from $NH_4^+$. Assuming this occurs via anammox, a corresponding 0.17 moles of $NO_2^-$ should also be converted to $N_2$. So, for every 1.17 moles of $N_2$-N produced, 0.34 moles, or 29% derives from anammox, which closely matches the expected overall contribution of anammox to biogenic $N_2$ production observed in the

ETSP (Dalsgaard et al., 2012), and that predicted based on organic matter stoichiometry (Devol, 2003; Babbin et al., 2014).

As can be seen from this discussion, both estimates of DIN deficit have their challenges. P released from sediments can lead to an overestimate of $[DIN]_{def,P}$ throughout the ODZ, while anammox leads to an underestimate of $[DIN]_{def,OMP}$ in the upper ODZ. In real terms, 0.3 μM $P_{xs,sed}$ in the middle ODZ is equivalent to about 5 μM $[DIN]_{def,P}$, which is similar to the underestimate of $[DIN]_{def,OMP}$, so both errors are of similar magnitude. Below, we discuss the sensitivity of the expressed isotope effects for $NO_3^-$ reduction and DIN removal on these uncertainties.

*$^{15}\varepsilon_{NAR}$, $^{18}\varepsilon_{NAR}$ and $^{15}\varepsilon_{DIN\text{-}R}$ variations with depth*

As observed in previous studies, use of different estimates for $[DIN]_{def}$ had a limited effect on estimates of $^{15}\varepsilon_{NAR}$, $^{18}\varepsilon_{NAR}$, and $^{15}\varepsilon_{DIN\text{-}R}$ (Table 1; Bourbonnais et al., 2015; Hu et al., 2016). A more significant bias can result from aerobic respiration along isopycnals as water flows from its origin to the ODZs, which can alter the apparent *f* value and the observed $\delta^{15}N_{NO3}$ depending on the isotopic composition of the remineralized N (Marconi et al., 2017). If one assumes that the deep water in a particular location is the source of water to the ODZ one may considerably overestimate the isotope effect for N loss (Marconi et al., 2017). In this study, we did calculate the apparent isotope effects across isopycnal surfaces for comparison to prior studies (Figure S5), but the bulk our analysis was along isopycnal surfaces (Table 1). Moreover, our estimates of $[DIN]_{def}$ account for aerobic respiration that occurred prior to entering the ODZ, and we make no assumptions about the $\delta^{15}N$ of initial $NO_3^-$. Still, we observed a range of apparent $^{15}\varepsilon_{NAR}$ values between 18.5-34.6‰ and $^{15}\varepsilon_{DIN\text{-}R}$ between 8.6 and 35.8‰ that varied considerably with depth. The isotope effects generally increased with depth (density) in the water column, and $^{15}\varepsilon_{DIN\text{-}R}$ was generally lower than $^{15}\varepsilon_{NAR}$ (Table 1). Regardless of which method was used to calculate *f*, the largest difference between $^{15}\varepsilon_{NAR}$ and $^{15}\varepsilon_{DIN\text{-}R}$ (with $^{15}\varepsilon_{DIN\text{-}R}$ significantly smaller than $^{15}\varepsilon_{NAR}$, $p = 0.02$) was found at $\sigma_\theta$ = 26.4-26.5 kg $m^{-3}$, within the upper part of the secondary $NO_2^-$ maximum (Figure 4).

The increase in $^{15}\varepsilon_{NAR}$ estimates at greater densities was also observed by Casciotti et al. (2013) in the ETSP ODZ, and was attributed to effects caused by $NO_2^-$ oxidation. Bourbonnais et

al. (2015) also attributed differences in $^{15}\varepsilon_{NAR}$ and $^{15}\varepsilon_{DIN\text{-}R}$ to $NO_2^-$ oxidation, arguing that the inverse isotope effect for $NO_2^-$ oxidation could drive $^{15}\varepsilon_{NAR}$ to be higher than $^{15}\varepsilon_{DIN\text{-}R}$ due to enrichment of $NO_3^-$ in $^{15}N$. Using a different method of $^{15}\varepsilon_{DIN\text{-}R}$ estimation, Fuchsman et al. (2017) examined the magnitude and distribution of apparent isotope effects with depth in the ETNP and found patterns that parallel those shown here—the largest isotope effects found in the middle ODZ, decreasing to shallower depths in the ODZ. However, they argued against $NO_2^-$ oxidation as the primary driver of depth differences in apparent isotope effects.

In the present study, this pattern was examined using the time-dependent model developed by Casciotti et al. (2013) to determine whether the differences between $^{15}\varepsilon_{NAR}$ and $^{15}\varepsilon_{DIN\text{-}R}$, and their variations with depth in the water column, could be explained by the activity of $NO_2^-$ oxidation or the accumulation of $NO_2^-$ in the water column. The model was admittedly simple, but it allowed us to dissect potential controlling factors in the expression of isotope effects in these systems. Briefly, this model allows $NO_3^-$ and $NO_2^-$ concentrations and isotope ratios to evolve in ODZ conditions from background conditions outside the ODZ, using a combination of $NO_3^-$ reduction, $NO_2^-$ reduction, and $NO_2^-$ oxidation. Prescribed N and O isotope effects for each of those processes allowed comparison of modeled $NO_3^-$ and $NO_2^-$ isotopic compositions to those observed (Casciotti et al., 2013). Model output for each scenario was used to calculate the apparent $^{15}\varepsilon_{NAR}$ and $^{15}\varepsilon_{DIN\text{-}R}$ using different process rates and isotope effects. By altering the rates of the N cycle processes in different scenarios (Table 2), we examined the influence of $NO_2^-$ oxidation and $NO_2^-$ accumulation on the expressed $^{15}\varepsilon_{NAR}$ and $^{15}\varepsilon_{DIN\text{-}R}$ values along isopycnal surfaces in the ETSP ODZ.

In all scenarios tested, the first order rate constant for $NO_3^-$ reduction ($k_{NAR}$) was set to 0.5 $yr^{-1}$ to achieve an appropriate $[DIN]_{def}$ over the model period (10 years), and the isotope effects were set to 12‰ for $^{15}\varepsilon_{NAR}$, 0‰ for $^{15}\varepsilon_{NIR}$, and -32‰ for $^{15}\varepsilon_{NXR}$ (Table 2). This isotope effect for $NO_3^-$ reduction is at the low end of literature values, but is consistent with recent estimates from a variety of approaches (Marconi et al., 2017; Casciotti et al., 2013; Krittee et al., 2012). The isotope effect for $NO_2^-$ reduction was recently determined in culture to range from 8-22‰ (Martin and Casciotti, 2016), but it is uncertain whether this isotope effect is expressed fully in the field (Casciotti et al., 2013; Bourbonnais et al., 2015; Peters et al., 2016). The isotope effect for $NO_2^-$ oxidation is more extreme than those measured in cultures of $NO_2^-$ oxidizing bacteria (Casciotti, 2009; Buchwald and Casciotti, 2010) but is consistent with $NO_2^-$ oxidation

711 during anammox (Brunner et al., 2013). The values used here for most of the scenarios were
712 optimized to fit $NO_3^-$ and $NO_2^-$ isotope data from the ETSP ODZ collected previously (Casciotti
713 et al., 2013), but the sensitivity of our conclusions to these isotope effects was also tested and
714 will be discussed below.
715 In the first model scenario, the first order rate constant for $NO_2^-$ oxidation ($k_{NXR}$) was set
716 to zero and the first order rate constant for $NO_2^-$ reduction ($k_{NIR}$) was set to 0.5 $yr^{-1}$. The apparent
717 $^{15}\varepsilon_{NAR}$ and $^{15}\varepsilon_{DIN\text{-}R}$ values from the model output were 13.0‰ and 8.3‰, respectively (Table 2).
718 In this case, $^{15}\varepsilon_{NAR}$ was similar to the prescribed value (12.0‰) and $^{15}\varepsilon_{DIN\text{-}R}$ was 4.7‰ lower.
719 The maximum [$NO_2^-$] exceeded 15 μM, and $\delta^{15}N_{DIN}$ remained close to $\delta^{15}N_{NO2}$ (Figure 8A). The
720 apparent $^{15}\varepsilon_{DIN\text{-}R}$ closely matched the field data for the 26.4-26.5 $\sigma_\theta$ surface, but the modeled
721 $^{15}\varepsilon_{NAR}$ was lower than observed.
722 In model scenario II, $k_{NIR}$ was increased to 1 $yr^{-1}$ and the other parameters were kept the
723 same as scenario I. This resulted in lower [$NO_2^-$] accumulation and isotope effect estimates for
724 $NO_3^-$ reduction and DIN removal that were more similar to each other (13.0 and 12.2‰,
725 respectively; Table 2). Here, $\delta^{15}N_{DIN}$ was more similar to $\delta^{15}N_{NO3}$ because of the lower
726 accumulation of $NO_2^-$, and the higher $\delta^{15}N_{NO2}$ due to enhanced $NO_2^-$ reduction (Figure 8C).
727 While there was no isotope effect for $NO_2^-$ reduction in the model, removal of $NO_2^-$, which
728 comprises the 'lightest' fraction of the DIN pool, causes $\delta^{15}N_{NO2}$ and $\delta^{15}N_{DIN}$ to increase. Even
729 higher rates of $NO_2^-$ reduction ($k_{NIR}$ = 2 $yr^{-1}$; scenario VI, Table 2; Figure S9) gave still lower
730 accumulations of [$NO_2^-$] and smaller differences between isotope effects (13.0 vs. 12.9‰). Thus,
731 one factor that can generate differences between $^{15}\varepsilon_{NAR}$ and $^{15}\varepsilon_{DIN\text{-}R}$ is the accumulation of $NO_2^-$,
732 which lowers $^{15}\varepsilon_{DIN\text{-}R}$ relative to $^{15}\varepsilon_{NAR}$, even in the absence of $NO_2^-$ oxidation.
733 Scenario III introduced $NO_2^-$ oxidation, with a moderate rate constant of $k_{NXR} = k_{NIR} =$
734 0.5 $yr^{-1}$. This scenario had a similar overall rate of $NO_2^-$ removal as scenario II, and yielded
735 similar maximal $NO_2^-$ accumulations (10.8 vs. 11.6 μM; Table 2). However, the introduction of
736 $NO_2^-$ oxidation caused the apparent isotope effects to increase dramatically, to 25.6 and 23.3‰,
737 respectively, and it increased the difference between $^{15}\varepsilon_{NAR}$ and $^{15}\varepsilon_{DIN\text{-}R}$ due mainly to the lower
738 $\delta^{15}N_{NO2}$ values, which lowered $\delta^{15}N_{DIN}$, and $^{15}\varepsilon_{DIN\text{-}R}$ relative to $^{15}\varepsilon_{NAR}$ (Figure 8F; Table 2).
739 Similar results were observed with $^{15}\varepsilon_{NXR}$ = -13‰, but to a lesser degree (Scenario VIII; Figure
740 S9). As discussed previously (Casciotti et al., 2013), the apparent $^{15}\varepsilon_{NAR}$ value exceeded the

741 prescribed value when $NO_2^-$ oxidation was active. However, it should be noted that the larger
742 $^{15}\varepsilon_{NAR}$ occurred due to a smaller change in *f* for a given amount of $NO_3^-$ reduction (ln(*f*)
743 decreased more slowly), rather than increased $\delta^{15}N_{NO3}$ (Figure S10).
744 When $NO_2^-$ reduction was eliminated ($NO_2^-$ oxidation served as the only $NO_2^-$ sink—
745 scenario V), [$NO_3^-$] decreased and [$NO_2^-$] increased to 20 μM (Table 2). Here, $\delta^{15}N_{NO3}$ reached
746 30.5‰, but $^{15}\varepsilon_{NAR}$ appeared larger (38.1‰) than the other scenarios due to the low apparent
747 $NO_3^-$ removal. [DIN] and $\delta^{15}N_{DIN}$ did not change (Figure S9) so $^{15}\varepsilon_{DIN\text{-}R}$ could not be calculated.
748 Thus, including $NO_2^-$ reduction is necessary to reproduce observed changes in DIN.
749 Increasing the rates of both $k_{NXR}$ and $k_{NIR}$ to 1 $yr^{-1}$ in scenario IV yielded one of the
750 lowest [$NO_2^-$] accumulations (7.3 μM), and a relatively small difference between $^{15}\varepsilon_{NAR}$ and
751 $^{15}\varepsilon_{DIN\text{-}R}$, though they were both elevated to near 27‰, with only 0.7‰ difference between them
752 (Table 2). Here, the elevated rate of $NO_2^-$ reduction increased $\delta^{15}N_{NO2}$, $\delta^{15}N_{NO3}$, and
753 consequently $\delta^{15}N_{DIN}$ above those observed in scenario III.
754 The prescribed isotope effects for $NO_2^-$ reduction, $NO_2^-$ oxidation, and $NO_3^-$ reduction
755 were varied in scenarios VII, VIII, and IX (and X), respectively. When using the rate constants
756 from scenario I (with no $NO_2^-$ oxidation) but raising the isotope effect for $NO_2^-$ reduction from
757 0‰ to 10‰, the apparent $^{15}\varepsilon_{NAR}$ remained at 13.0‰, but $^{15}\varepsilon_{DIN\text{-}R}$ increased to 15.3‰ (Table 2).
758 This was the only scenario that resulted in $^{15}\varepsilon_{DIN\text{-}R}$ exceeding $^{15}\varepsilon_{NAR}$, which was not observed at
759 any density in the ETSP ODZ. When the isotope effect for $NO_3^-$ reduction was increased to 25‰
760 from the base case, the apparent $^{15}\varepsilon_{NAR}$ increased to 27.7‰, while $^{15}\varepsilon_{DIN\text{-}R}$ increased to only
761 17.4‰ (Scenario IX; Table 2). This scenario resulted in the largest difference between $^{15}\varepsilon_{NAR}$
762 and $^{15}\varepsilon_{DIN\text{-}R}$ (10.3‰). Finally, when $NO_2^-$ oxidation was added in to scenario X with the
763 prescribed $^{15}\varepsilon_{NAR}$ = 25‰, the apparent $^{15}\varepsilon_{NAR}$ increased to 35.9‰ and $^{15}\varepsilon_{DIN\text{-}R}$ increased to
764 33.2‰.
765 These model results suggest that the activity of $NO_2^-$ oxidation can affect the differences
766 between $^{15}\varepsilon_{DIN\text{-}R}$ and $^{15}\varepsilon_{NAR}$, through changes in $\delta^{15}N_{NO3}$ and $\delta^{15}N_{NO2}$ as well as the relative
767 contributions of $NO_2^-$ and $NO_3^-$ to the DIN pool. However, the effect of $NO_2^-$ oxidation is not
768 simple. In order to explain the increase in $^{15}\varepsilon_{NAR}$ values at greater densities, a relatively stronger
769 influence from $NO_2^-$ oxidation in the lower ODZ, as well as a higher inherent isotope effect for
770 $NO_3^-$ reduction were needed. This might be expected due to the lower organic matter supply

771 favoring autotrophic processes and slowing down the rates of $NO_3^-$ reduction. Autotrophic
772 processes such as $NO_2^-$ oxidation (either by anammox or $NO_2^-$-oxidizing bacteria) are not
773 dependent upon the organic matter supply, and can thus become relatively more important when
774 heterotrophic processes become limited. In support of this, we found that the $\delta^{15}N$ difference
775 between $NO_3^-$ and $NO_2^-$ ($\Delta\delta^{15}N = \delta^{15}N_{NO3} - \delta^{15}N_{NO2}$; Casciotti, 2009) increased with depth in the
776 ODZ, and the apparent $^{15}\varepsilon_{NAR}$ values throughout the ODZ exceeded those of $^{18}\varepsilon_{NAR}$ (Table 1).
777 While the $^{15}\varepsilon_{NAR}$ and $^{18}\varepsilon_{NAR}$ values are expected to be the same if $NO_3^-$ reduction is the only
778 process acting upon $\delta^{15}N_{NO3}$ and $\delta^{18}O_{NO3}$ (Sigman et al., 2005; Granger et al., 2008), one
779 mechanism that has been hypothesized to generate a mismatch between $^{15}\varepsilon_{NAR}$ and $^{18}\varepsilon_{NAR}$ is the
780 reoxidation of $NO_2^-$ to $NO_3^-$ (Sigman et al., 2005; Casciotti and McIlvin, 2007). Casciotti (2016)
781 used this model to demonstrate that $NO_2^-$ oxidation can cause $\delta^{18}O_{NO3}$ to decrease relative to
782 $\delta^{15}N_{NO3}$ when $\delta^{15}N_{NO3}$ and $\delta^{18}O_{NO3}$ values are greater than 10 to 15‰. Thus, our analysis
783 provides further support that $NO_2^-$ oxidation is influencing the waters of the ETSP ODZ and
784 corroborates the presence and activity of $NO_2^-$ oxidizing bacteria there (Ward et al., 1989;
785 Lipschultz et al., 1990; Peng et al., 2016; Babbin et al., 2017). However, from our simple model
786 analysis, the large $^{15}\varepsilon_{NAR}$ and $^{15}\varepsilon_{DIN\text{-}R}$ values in the lower ODZ most likely resulted from a
787 mixture of $NO_2^-$ oxidation and reduction that raise $^{15}\varepsilon_{NAR}$ and $^{15}\varepsilon_{DIN\text{-}R}$ where $NO_2^-$ accumulation
788 is less (Table 2).
789
790 *Relationship between $\delta^{15}N_{N2,bio}$ and $\delta^{15}N_{NO2}$*
791 $\delta^{15}N_{N2,bio}$ and $\delta^{15}N_{NO2}$ were remarkably similar within the ODZ (Figure 7), which was
792 surprising given that biogenic $N_2$ is produced from $NO_2^-$ via denitrification and anammox under
793 low $O_2$ conditions. Given this, it might be expected that $\delta^{15}N_{N2,bio}$ would generally be lower than
794 $\delta^{15}N_{NO2}$, given that previous field and laboratory studies have suggested that the N isotope effect
795 of $NO_2^-$ reduction may be 8-20‰ (Bryan et al., 1983; Bourbonnais et al., 2015; Martin and
796 Casciotti, 2016). Also, as there is no sink for $N_{2,bio}$, it should behave as an accumulated product,
797 while $NO_2^-$ is more dynamic, being simultaneously produced by $NO_3^-$ reduction and consumed
798 by $NO_2^-$ reduction and oxidation. In order to better understand the similarity between $\delta^{15}N_{N2,bio}$
799 and $\delta^{15}N_{NO2}$ we examined their behavior in results from the same time dependent model
800 discussed above (Casciotti et al. 2013).

We were unable to reproduce the close similarity of $\delta^{15}N_{N2,bio}$ and $\delta^{15}N_{NO2}$ using $^{15}\varepsilon_{NIR}$ values of 10‰ to 20‰ (not shown). The model could only achieve a tight coupling of $\delta^{15}N_{N2,bio}$ and $\delta^{15}N_{NO2}$ when the isotope effect for $NO_2^-$ reduction was negligible (< 5‰). Thus, $\delta^{15}N_{N2}$ data support the low expression of $^{15}\varepsilon_{NIR}$ in the environment, consistent with the use of an $NO_2^-$ reduction isotope effect of 0‰ throughout the main model runs (Table 2). Increasing the N isotope effect for $NO_2^-$ reduction to values of 10 to 20‰ (that is, those values suggested by lab and field studies) only drives $\delta^{15}N_{N2,bio}$ and $\delta^{15}N_{NO2}$ values farther apart in the model. This suggests that the isotope effect for $NO_2^-$ reduction that is actually expressed in the ODZ may be lower than the inherent fractionation factors observed in culture, and further points to a need for both field and laboratory studies when examining marine N cycle isotope effects.

## Conclusions

In this study, we found that the DIN deficit calculated using $[PO_4^{3-}]$ in the ETSP exceeded the local biogenic $[N_2]$. This could best be explained by release of $PO_4^{3-}$ from coastal sediments. Our estimates of 'excess' $[PO_4^{3-}]$ ranged between 0.2 and 0.6 μM, and could explain up to 9.5 μM of apparent DIN deficit. Thus, we recommend that caution be taken when using $[PO_4^{3-}]$ measurements to estimate fixed N loss within ODZs, especially in areas affected by sediments. Furthermore, we present an alternative method for calculating the DIN deficit from a water mass analysis, together with nutrient and oxygen measurements, which may provide a better estimate of $N_2$ production where sedimentary $[PO_4^{3-}]$ release is a factor. Estimation of the DIN deficit from OMPA yielded better agreement with $[N_2]_{bio,local}$ in the lower ODZ but not in the upper part of the ODZ, where anammox plays a significant role in biogenic $N_2$ production. Here, $[DIN]_{def,OMP}$ underestimated $[N_2]_{bio,local}$ by 17%.

It was found that both $^{18}\varepsilon_{NAR}$ and $^{15}\varepsilon_{DIN\text{-}R}$ values were lower than $^{15}\varepsilon_{NAR}$, which is consistent with $NO_2^-$ oxidation and reduction together acting upon the isotopes of $NO_3^-$ and $NO_2$. Using the time-dependent ODZ model developed by Casciotti et al. (2013), it was revealed that the accumulation of $NO_2^-$ in addition to the action of $NO_2^-$ oxidation likely drove the differences among $^{15}\varepsilon_{DIN\text{-}R}$ and $^{15}\varepsilon_{NAR}$ estimates with depth in the ODZ, although variation in $^{15}\varepsilon_{NAR}$ with depth may also play a role. $NO_2^-$ oxidation increased the apparent values of both $^{15}\varepsilon_{NAR}$ and $^{15}\varepsilon_{DIN\text{-}R}$, amplifying the effects of $NO_2^-$ accumulation on the differences between the two isotope effects.

Lastly, we found that estimates of biogenic $\delta^{15}N_{N2}$ roughly matched $\delta^{15}N_{NO2}$ throughout the ODZ. Modeling experiments suggested that this coupling of $\delta^{15}N_{N2}$ and $\delta^{15}N_{NO2}$ was likely driven by a greater influence of $NO_2^-$ oxidation deeper in the ODZ, which was needed to achieve the low $\delta^{15}N_{NO2}$ values. These comparisons, however, are dependent upon $\delta^{15}N_{N2,bio}$ measurements, which demonstrated a relatively high degree of uncertainty. Tighter constraints on $\delta^{15}N_{N2,bio}$ measurements could help strengthen these conclusions, and may greatly enhance our understanding of fixed N loss, along with the DIN deficit and biogenic [$N_2$] measurements.

**Acknowledgements**

We greatly thank Dr. Bess Ward as well as the Captain and crew of the R/V Nathaniel B. Palmer for a successful cruise. We also thank the two anonymous reviewers for their insightful and constructive comments on the manuscript. This research was funded by NSF-OCE through grants 1140404 to KLC, 1046017 to AHD, and 1233425 to CWM. This publication was also partially funded by the Joint Institute for the Study of the Atmosphere and Ocean (JISAO) under NOAA Cooperative Agreement NA10OAR4320148, and is contribution 2017-0102 to JISAO and contribution 4614 to NOAA's Pacific Marine Environmental Laboratory. The hydrographic data from this cruise is publicly available and can be obtained by accessing the url: http://data.nodc.noaa.gov/cgi-bin/iso?id=gov.noaa.nodc:0128141.

**REFERENCES**


Anderson, L. A. 1995. On the hydrogen and oxygen content of marine phytoplankton. Deep Sea Res I 42, 1675-1680. doi:10.1016/0967-0637(95)00072E.

Anderson, L. A., Sarmiento, J. L. 1994. Redfield ratios of remineralization determined by nutrient data analysis. Glob Biogeochem Cycles 8, 65-80.

Arrigo, K. R. 2005. Marine microorganisms and global nutrient cycles. Nature 437, 349-355.

Babbin, A. R., Keil, R. G., Devol, A. H., Ward, B. B. 2014. Organic matter stoichiometry, flux, and oxygen control nitrogen loss in the ocean. Science 344, 406-408.

Babbin, A.R., Peters, B.D., Mordy, C.W., Widner, B., Casciotti, K.L., Ward, B.B. 2017. Multiple metabolisms constrain the anaerobic nitrite budget in the Eastern Tropical South Pacific. Glob Biogeochem Cycles 31, 258-271.

Bianchi, D., Babbin, A.R., Galbraith, E.D. 2014. Enhancement of anammox by the excretion of diel vertical migrators. Proc. Natl. Acad. Sci. 111,15653-15658.

Bostock, H.C., Opdyke, B.N., Williams, M.J. 2010. Characterising the intermediate depth waters of the Pacific Ocean using $\delta^{13}C$ and other geochemical tracers. Deep Sea Res I 57, 847-859.

Bourbonnais, A., Altabet, M. A., Charoenpong, C. N., Larkum, J., Hu, H., Bange, H. W., Stramma, L. 2015. N-loss isotope effects in the Peru oxygen minimum zone studied using a mesoscale eddy as a natural tracer experiment. Glob Biogeochem Cycles 29, 793-811. Doi: 10.1002/2014GB005001.

Brandes, J.A. and Devol, A.H. 1997. Isotopic fractionation of oxygen and nitrogen in coastal marine sediments. Geochim. Cosmochim. Acta 61, 1793-1801.

Brandes, J.A., Devol, A.H. 2002. A global marine-fixed nitrogen isotopic budget: Implications for Holocene nitrogen cycling. Glob Biogeochem Cycles, 16.

Broecker, W. S., & Peng, T. H. 1982. Tracers in the Sea, 690 pp. *Lamont-Doherty Geological Observatory, Palisades, NY*

Brunner, B., Contreras, S., Lehmann, M.F., Matantseva, O., Rollog, M., Kalvelage, T., Klockgether, G., Lavik, G., Jetten, M., Kartal, B., Kuypers, M.M. 2013. Nitrogen isotope effects induced by anammox bacteria. Proc of the Nat Acad of Sci 110, 18994-18999. doi:10.1073/pnas.1310488110.

Bryan, B.A., Shearer, G., Skeeters, J.L., Kohl, D.H. 1983. Variable expression of the nitrogen isotope effect associated with denitrification of nitrite. J of Biol Chem 258, 8613-8617.

Buchwald, C. and Casciotti, K.L. 2010. Oxygen isotopic fractionation and exchange during bacterial nitrite oxidation. Limnol. Oceanog. 3, 1064-1074.

Buchwald, C., Santoro, A. E., Stanley, R. H., Casciotti, K. L. 2015. Nitrogen cycling in the secondary nitrite maximum of the eastern tropical North Pacific off Costa Rica. Global Biogeochemical Cycles, 29, 2061-2081. doi: 10.1002/2015GB005187.

Canfield, D.E, Stewart, F.J., Thamdrup, B., De Brabandere, L., Dalsgaard, T., Delong, E.F., Revsbech, N.-P., Ulloa, O. 2010. A cryptic sulfur cycle in oxygen minimum zone waters off the Chilean coast. Science. 330, 1375-1378.

Casciotti, K.L., Sigman, D.M., Hastings, M.G., Bohlke, J.K., Hilkert, A. 2002. Measurements of the oxygen isotopic composition of nitrate in seawater and freshwater using the denitrifier method. Anal. Chem. 74, 4905 – 4912. doi: 10.1021/ac020113w.

Casciotti, K.L., and McIlvin, M.R. 2007. Isotopic analyses of nitrate and nitrite from reference mixtures and application to Eastern Tropical North Pacific waters. Mar. Chem. 107, 184-201.

Casciotti, K.L. 2009. Inverse kinetic isotope fractionation during bacterial nitrite oxidation. Geochim. Cosmochim. Acta 73, 2061 – 2076. doi: 10.1016/j.gca.2008.12.022

Casciotti, K.L., Buchwald, C., McIlvin, M. 2013. Implications of nitrate and nitrite isotope measurements for the mechanisms of nitrogen cycling in the Peru oxygen deficient zone. Deep Sea Res. I 80, 78-93. doi: 10.1016/j.dsr.2013.05.017

Casciotti, K.L. 2016. Nitrite isotopes as tracers of marine N cycle processes. Phil. Trans. A. 374, 20150295.

Chang, B.X., Devol, A.H., Emerson, S.R. 2010. Denitrification and the nitrogen gas excess in the eastern tropical South Pacific oxygen deficient zone. Deep Sea Res I 57, 1092-1101.

Chang, B.X., Devol, A.H., Emerson, S.R., 2012. Fixed nitrogen loss from the eastern tropical North Pacific and Arabian Sea oxygen deficient zones determined from measurements of N2: Ar. Glob Biogeochem Cyc, 26.

Chang, B. X., Rich, J. R., Jayakumar, A., Naik, H., Pratihary, A. K., Keil, R. G., Ward, B.B., Devol, A. H. 2014. The effect of organic carbon on fixed nitrogen loss in the eastern tropical South Pacific and Arabian Sea oxygen deficient zones. Limnol Oceanogr 59, 1267 – 1274.

Chavez, F., Messie, M. 2009. A comparison of Eastern Boundary Upwelling Ecosystems. Prog. Oceanogr. 83, 80 – 96. doi:10.1016/j.pocean.2009.07.032

Cline, R.D., Richards, F.A. 1972. Oxygen deficient conditions and nitrate reduction in the eastern tropical ocean. Limnol. Oceanogr. 17, 885 – 900. doi: 10.4319/lo.1972.17.6.0885.

Codispoti, L.A., Christensen, J.P. 1985. Nitrification, denitrification, and nitrous oxide cycling in the eastern tropical south pacific ocean. Mar. Chem. 16, 277 – 300. doi: 10.1016/0304-4203(85)90051-9.

Codispoti, L. A., Brandes, J. A., Christensen, J. P., Devol, A. H., Naqvi, S. W. A., Paerl, H. W., and Yoshinari, T. 2001. The oceanic fixed nitrogen and nitrous oxide budgets: Moving targets as we enter the anthropocene? Scientia Marina 65, 85-105.

Czeschel, R., Stramma, L., Schwarzkopf, F. U., Giese, B. S., Funk, A., Karstensen, J. 2011. Middepth circulation of the eastern tropical South Pacific and its link to the oxygen minimum zone. J. Geophys Res. 116, C01015. doi: 10.1029/2010JC006565.

Dalsgaard, T., Canfield, D. E., Petersen, J., Thamdrup, B., and Acuña-González, J. 2003. $N_2$ production by the anammox reaction in the anoxic water column of Golfo Dulce, Costa Rica. Nature 422, 606-608.

Dalsgaard, T., Thamdrup, T., and Canfield, D.E. 2005. Anaerobic ammonium oxidation (anammox) in the marine environment. Res. Microbiol. 156, 457-464.

Dalsgaard, T., Thamdrup, T., Farias, L., and Revsbech, N.-P. 2012. Anammox and denitrification in the oxygen minimum zone of the eastern South Pacific. Limnol. Oceanog. 57, 1331-1346.

Deutsch, C., Sigman, D.M., Thunell, R.C., Meckler, A.N., and Haug, G.H. 2004. Isotopic constraints on glacial/interglacial changes in the oceanic nitrogen budget. Glob. Biogeochem. Cyc. 18, GB4012.

Devol, A.H. 2003. Solution to a marine mystery. Nature 422, 575-576.

DeVries, T., Deutsch, C., Primeau, F., Chang, B., Devol, A. 2012. Global rates of water-column denitrification derived from nitrogen gas measurements. Nature Geoscience 5, 547-550.

DeVries, T., Deutsch, C., Rafter, P.A., Primeau, F., 2013. Marine denitrification rates determined from a global 3-D inverse model. Biogeosciences, 10.

Emerson, S., Stump, C., Wilbur, D., Quay, P. 1999. Accurate measurement of $O_2$, $N_2$, and Ar gases in water and the solubility of $N_2$. Mar Chem 64, 337-347.

Escribano, R., Daneri, G., Farías, L., Gallardo, V.A., González, H.E., Gutiérrez, D., Lange, C.B., Morales, C.E., Pizarro, O., Ulloa, O. Braun, M. 2004. Biological and chemical consequences of the 1997–1998 El Niño in the Chilean coastal upwelling system: a synthesis. Deep Sea Res II 51, 2389-2411.

Fiedler, P.C., Talley, L.D. 2006. Hydrography of the eastern tropical Pacific: A review. Prog. Oceanogr. 69, 143 – 180.

Franz, J., Hauss, H., Sommer, U., Dittmar, T., Riebesell, U. 2012. Production, partitioning and stoichiometry of organic matter under variable nutrient supply during mesocosm experiments in the tropical Pacific and Atlantic Ocean. Biogeosciences 9, 4629-4643.

Fuchsman, C. A., Murray, J. W., Konovalov, S. K. 2008. Concentration and natural stable isotope profiles of nitrogen species in the Black Sea. Mar Chem 111, 90-105.

Fuchsman, C.A., Devol, A.H., Casciotti, K.L., Buchwald, C., Chang, B.X., and Horak, R. E. A. 2017. An N isotopic mass balance of the Eastern Tropical North Pacific Oxygen Deficient Zone. Deep Sea Res. II. https://doi.org/10.1016/j.dsr2.2017.12.013.

Fuenzalida, R., Schneider, W., Garcés-Vargas, J., Bravo, L., Lange, C.. 2009. Vertical and horizontal extension of the oxygen minimum zones in the eastern South Pacific Ocean. Deep Sea Res II. 56, 992 – 10003.

Gehrie, E., Archer, D., Emerson, S., Stump, C., Henning, C. 2006. Subsurface ocean argon disequilibrium reveals the equatorial Pacific shadow zone. *Geophys Res Lett 33*.

Glover, D.M., Jenkins, W.J., Doney, S.C. 2011. Modeling Methods for Marine Science. Cambridge University Press, Cambridge, U.K.

Gordon, L. I., Jennings, J. C., Jr., Ross, A. A., Krest, J. M. 1993. A suggested Protocol for Continuous Flow Automated Analysis of Seawater Nutrients in the WOCE Hydrographic Program and the Joint Global Ocean Fluxes Study," Grp. Tech Rpt 92-1, OSU College of Oceanography Descr. Chem Oc.

Granger, J., Sigman, D. M., Lehmann, M. F., Tortell, P. D. 2008. Nitrogen and oxygen isotope fractionation during dissimilatory nitrate reduction by denitrifying bacteria. Limnol and Oceanogr 53, 2533-2545.

Granger, J. Sigman, D.M. 2009. Removal of nitrite with sulfamic acid for nitrate N and O isotope analysis with the denitrifier method. Rapid Commun. Mass Spectrom. 23, 3753 – 3762.

Grasse, P., Stichel, T., Stumpf, R., Stramma, L., Frank, M. 2012. The distribution of neodymium isotopes and concentrations in the Eastern Equatorial Pacific: Water mass advection versus particle exchange. Earth Planet Sci. Let. 354-353, 198 - 207.

Grasse, P., Ehlert, C., Frank, M. 2013. The influence of water mass mixing on the dissolved Si isotope composition in the Eastern Equatorial Pacific. Earth Planet Sci. Let. 380, 60 - 71.

Grosskopf, T., Mohr, W., Baustian, T., Schunck, H., Gill, D., Kuypers, M.M., Lavik, G., Schmitz, R.A., Wallace D.W.R., LaRoche, J. 2012. Doubling of marine dinitrogen-fixation rates based on direct measurements. Nature 488, 361-364.

Gruber, N. and Sarmiento, J.L. 1997. Global patterns of marine nitrogen fixation and denitrification. Glob. Biogeochem. Cyc. 11, 235-266.

Henning, C. C., Archer, D., Fung, I. 2006. Argon as a tracer of cross-isopycnal mixing in the thermocline. J Phys Oceanogr 36, 2090-2105.

Hu, H., Bourbonnais, A., Larkum, J., Bange, H.W., Altabet, M.A. 2016. Nitrogen cycling in shallow low-oxygen coastal waters off Peru from nitrite and nitrate nitrogen and oxygen isotopes. Biogeosciences 13, 1453 – 1468. doi: 10.5194/bg-13-1453-2016.

Ito, T., Follows, M.J., and Boyle, E.A. 2004. Is AOU a good measure of respiration in the oceans? Geophys. Res. Lett. 31, L17305.

Ito, T., Deutsch, C., Emerson, S., Hamme, R. C. 2007. Impact of diapycnal mixing on the saturation state of argon in the subtropical North Pacific. Geophys Res Lett 34.

Jayakumar, A., Chang, B.X., Widner, B., Bernhardt, P., Mulholland, M.R., and Ward, B.B. 2017. Biological nitrogen fixation in the oxygen-minimum region of the eastern tropical North Pacific ocean. ISME J. 11, 2356-2367.

Jenkins, W.J., Smethie, W.M., Boyle, E.A., Cutter, G.A. 2015. Water mass analysis for the U.S. GEOTRACES (GA03) North Atlantic sections. Deep Sea Res. II 116, 6 – 20.

Jensen, M.M., Lam, P., Revsbech, N.P., Nagel, B., Gaye, B., Jetten, M.S.M, and Kuypers, M.M.M. 2011. Intensive nitrogen loss over the Omani Shelf due to anammox coupled with dissimilatory nitrite reduction to ammonium. ISME J. 5, 1660-1670.

Kalvelage, T., Lavik, G., Lam, P., Contreras, S., Arteaga, L., Löscher, C.R., Oschlies, A., Paulmier, A., Stramma, L. and Kuypers, M.M. 2013. Nitrogen cycling driven by organic matter export in the South Pacific oxygen minimum zone. Nature Geoscience 6, 228-234.

Karstensen, J., Stramma, L., Visbeck, M. 2008. Oxygen minimum zones in the eastern tropical Atlantic and Pacific oceans. Prog. Oceanogr. 77, 331 – 350.

Kessler, W. S. 2006. The circulation of the eastern tropical Pacific: A review. Prog. Oceanogr. 69, 181 – 217.

Klots, C. E., Benson, B.B. 1963. Isotope effect in the solution of oxygen and nitrogen in distilled water. J Chem Phys 38, 890-892.

Knox, M., Quay, P.D., Wilbur, D. 1992. Kinetic isotopic fractionation during air-water gas transfer of $O_2$, $N_2$, $CH_4$, and $H_2$. J Geophys Res Oceans 97, 20335-20343.

Koeve, K., Kahler, P. 2010. Heterotrophic denitrification vs. autotrophic anammox – quantifying collateral effects on the oceanic carbon cycle. Biogeosciences 7, 2327 – 2337. doi: 10.5194/bg-7-2327-201.

Kritee, K., Sigman, D.M., Granger, J., Ward, B.B., Jayakumar, A., Deutsch, C. 2012. Reduced isotope fractionation by denitrification under conditions relevant to the ocean. Geochim Cosmochim Acta 92, 243-259.

Lam, P., Lavik, G., Jensen, M.M., van de Vossenberg, J., Schmid, M., Woebken, D., Gutierrez, R., Amann, M.S.M., Kuypers, M.M. 2009. Revising the nitrogen cycle in the Peruvian oxygen minimum zone. Proc. Natl. Acad. Sci. 106, 4752 – 4757. doi: 10.1073/pnas.0812444106.

Langdon, C. 2010. Determination of dissolved oxygen in seawater by Winkler titration using the amperometric technique. IOCCP Report No. 14.

Lehmann, M.F., Sigman, D.M., and Berelson, W.M. 2004. Coupling the $^{15}N/^{14}N$ and $^{18}O/^{16}O$ of nitrate as a constraint on benthic nitrogen cycling. Mar. Chem. 88, 1-20.

Lehmann, M.F., Sigman, D.M., McCorkle, D.C., Granger, J., Hoffmann, S., Cane, G., and Brunelle, B.G. 2007. The distribution of nitrate $^{15}N/^{14}N$ in marine sediments and the impact of benthic nitrogen loss on the isotopic composition of oceanic nitrate. Geochim. Cosmochim. Acta. 71, 5384-5404.

Lipschultz, F., Wofsy, S.C., Ward, B.B., Codispoti, L.A., Friedrich, G. Elkins, J.W. 1990. Bacterial transformations of inorganic nitrogen in the oxygen-deficient waters of the Eastern Tropical South Pacific Ocean. Deep-Sea Res. 37, 1531 – 1541.

Llanillo, P.J., Karstensen, J., Pelegrí, J.L., Stramma, L. 2013. Physical and biogeochemical forcing of oxygen and nitrate changes during El Nino/El Viejo and La Nina/La Vieja upper-ocean phases in the tropical eastern South Pacific along 86°W. Biogeosciences 10, 6339 – 6355. DOI: 10.5194/bg-10-633-2013.

Loescher, C.R., Grosskopf, T., Desai, F.D., Gill, D. Schunck, H., Croot, P.L., Schlosser, C., Neulinger, S.C., Pinnow, N., Lavik, G., Kuypers, M.M.M., LaRoche, J., and Schmitz, R.A. 2014. Facets of diazotrophy in the oxygen minimum zone waters off Peru. ISME J. 8, 2180-2192.

Luyten, J.R., Pedlosky, J., Stommel, H. 1983. The Venilated Thermocline. J. Phys. Oceanogr. 13, 292 – 309.

Mackas, D.L., Denman, K.L., Bennet, A.F. 1987. Least Squares Multiple Tracer Analysis of Water Mass Composition. J. Geophys. Res. 92, 2907 – 2918.

Manning, C.C., Hamme, R.C., Bourbonnais, A. 2010. Impact of deep-water renewal events on fixed nitrogen loss from seasonally-anoxic Saanich Inlet. Marine Chemistry, 122, 1-10.

Mantoura, R.F.C., Woodward, E.M.S. 1983. Optimization of the indophenol blue method for the automated determination of ammonia in estuarine waters. Estuar. Coast. Shelf. Sci. 17, 219 – 224.

Marconi, D., Kopf, S., Rafter, P.A., and Sigman, D.M. 2017. Aerobic respiration along isopycnals leads to overestimation of the isotope effect of denitrification in the ocean water column. Geochim. Cosmochim. Acta. 197, 417-432.

Martin, T. S., Casciotti, K. L. (2016). Nitrogen and oxygen isotopic fractionation during microbial nitrite reduction. Limnol Oceanogr 61, 1134 – 1143.

Martiny, A.C., Pham, C.T., Primeau, F.W., Vrugt, J.A., Moore, J.K., Levin, S.A., Lomas, M.W. 2013. Strong latitudinal patterns in the elemental ratios of marine plankton and organic matter. Nature Geoscience 6, 279-283.

McIlvin, M.R., Altabet, M.A. 2005. Chemical conversion of nitrate and nitrite to nitrous oxide for nitrogen and oxygen isotopic analysis in freshwater and seawater. Anal. Chem. 77, 5589 – 5595. doi: 10.1021/ac050528s.

McIlvin, M.R., and Casciotti, K.L. 2011. Technical updates to the bacterial method for nitrate isotopic analyses. Anal. Chem. 83, 1850-1856.

Mills, M.M. and Arrigo, K.R. 2010. Magnitude of oceanic nitrogen fixation influenced by the nutrient uptake ratio of phytoplankton. Nat. Geosci. 3, 412-416.

Mills, M.M, Brown, Z.W., Lowry, K.E., van Dijken, G.L., Becker, S., Pal, S., Benitez-Nelson, C.R., Downer, M.M., Strong, A.L., Swift, J.H., Pickart, R.S., and Arrigo, K.R. 2015. Impacts of low phytoplankton $NO_3^-$:$PO_4^{3-}$ utilization ratios over the Chukchi Shelf, Arctic Ocean. Deep-Sea Res II. 118, 105-121.

Montes, I., Colas, F., Capet, X., Schneider, W. 2010. On the pathways of the equatorial subsurface currents in the eastern equatorial Pacific and their contributions to the Peru-Chile Undercurrent. J. Geophys. Res. 115, C09003. DOI 10.1029/2009JC005710.

Paulmier, A., Ruiz-Pino, D., Garcon, V., Farias, L. 2006. Maintaining of the Eastern South Pacific Oxygen Minimum Zone (OMZ) off Chile. Geophys. Res. Lett. 33, L20601.

Paulmier, A., Ruiz-Pino, D., Garçon, V. 2009. The oxygen minimum zones (OMZs) in the modern ocean. Prog. Oceanogr. 80, 113 – 128.

Peng, X., Fuchsman, C.A., Jayakumar, A., Warner, M.J., Devol, A.H., Ward, B.B. 2016. Revisiting nitrification in the Eastern Tropical South Pacific: a focus on controls. J Geophys Res: Oceans. 121, 1667 – 1684. Doi:10.1002/2015JC011455.

Penn, J., Weber, T., Deutsch, C. 2016. Microbial functional diversity alters the structure and sensitivity of oxygen deficient zones. Geophys Res Lett 43, 9773-9780.

Peters, B. D., Babbin, A. R., Lettmann, K. A., Mordy, C. W., Ulloa, O., Ward, B. B., Casciotti, K. L. 2016. Vertical modeling of the nitrogen cycle in the eastern tropical South Pacific oxygen deficient zone using high-resolution concentration and isotope measurements. Glob Biogeochem Cycles 30, 1661-1681.

Peters, B.D., Jenkins, W.J., Swift, J.H., German, C.R., Moffett, J.W., Cutter, G.A., Brzezinski, M.A., and Casciotti, K.L. 2017. Water mass analysis of the 2013 US GEOTRACES eastern Pacific zonal transect (GP16). Mar. Chem. https://doi.org/10.1016/j.marchem.2017.09.007.

Reid, J.L. 1973. The shallow salinity minima of the Pacific Ocean. Deep Sea Res 20, 51 – 68.

Redfield, A.C., Ketchum, B.H., Richards, F.A. 1963. in The Sea (ed. Hill, M.N.) Vol. 2, 26 – 77 (Interscience, New York, 1963).

Richards, F.A. 1965. Anoxic basins and fjords. In *Chemical Oceanography* Vol. 1, 611-645. Riley, J.P. and Skirrow, G., eds. Academic Press, New York.

Schneider, W., Fuenzalida, R., Rodriguez-Rubia, E., Garces-Vargas, J. 2003. Characteristics and formation of Eastern South Pacific Intermediate Water. Geophys. Res. Lett. 30, 1581. doi:10.1029/2003GL017086.

Sigman, D.M., Casciotti, K.L., Andreani, M., Barford, C., Galanter, M., Bohlke, J.K.. 2001. A bacterial method for the nitrogen isotopic analysis of nitrate in seawater and freshwater. Anal Chem. 73, 4145 – 4153.

Sigman, D.M., Robinson, R., Knapp, A.N., Van Geen, A., McCorkle, D.C., Brandes, J.A., Thunell, R.C., 2003. Distinguishing between water column and sedimentary denitrification in the Santa Barbara Basin using the stable isotopes of nitrate. Geochemistry, Geophysics, Geosystems, 4.

Sigman, D.M., Granger, J., DiFiore, P.J., Lehmann, M.M., Ho, R., Cane, G., van Geen, A., 2005. Coupled nitrogen and oxygen isotope measurements of nitrate along the eastern North Pacific margin. Glob Biogeochem Cyc 19.

Silva, N., Neshyba, S. 1979. On the southernmost extension of the Peru-Chile Undercurrent. Deep-Sea Res. 26A, 1387 – 1393.

Silva, N., Rojas, N., Fedele, A. 2009. Water masses in the Humboldt Current System: Properties, distribution, and nitrate deficit as a chemical water mass tracer for Equatorial Subsurface Water off Chile. Deep Sea Res. II 56, 1004 – 1020.

Somes, C.J., Oschlies, A., and Schmittner, A. 2013. Isotopic constraints on the pre-industrial oceanic nitrogen budget. Biogeosci. 10, 5889-5910.

Stramma, L., Johnson, G.C., Firing, E., Schmidtko, S. 2010. Eastern Pacific oxygen minimum zones: Supply paths and multidecadal changes. J. Geophys. Res. 115, C09011.

Strous, M., Heijnen, J.J., Kuenen, J.G., Jetten, M.S.M. 1998. The sequencing batch reactor as a powerful tool for the study of slowly growing anaerobic ammonium-oxidizing microorganisms. App microbiol biotechnol 50, 589-596.

Talley L.D., Pickard, G.L., Emery, W.J., Swift, J.H. 2011. Descriptive Physical Oceanography: An introduction (Sixth edition), Elsevier, Boston.

Thamdrup, B., Dalsgaard, T., Revsbech, N. P. 2012. Widespread functional anoxia in the oxygen minimum zone of the Eastern South Pacific. Deep Sea Res I 65, 36-45.

Tomczak, M., Large, D.G.B. 1989. Optimum Multiparameter Analysis of Mixing in the Thermocline of Eastern Indian Ocean. J. Geophys. Res. 94, 16141 – 16149.

Tsuchiya, M., Talley, L.D. 1998. A Pacific hydrographic section at 88° W : Water-property distribution. J. Geophys. Res. 103: 12899 – 12918.

Treibergs, L.A., Fawcett, S.E., Lomas, M.W., Sigman, D.M., 2014. Nitrogen isotopic response of prokaryotic and eukaryotic phytoplankton to nitrate availability in Sargasso Sea surface waters. Limnol and Oceanogr 59, 972-985.

Ulloa, O., Pantoja, S. 2009. The oxygen minimum zone of the eastern South Pacific. Deep Sea Res II 56, 987 – 991.

Van de Graaf, A.A., de Bruijn, P., Robertson, L.A., Jetten, M.S., Kuenen, J.G., 1996. Autotrophic growth of anaerobic ammonium-oxidizing micro-organisms in a fluidized bed reactor. Microbiology 142, 2187-2196.

Van Mooy, B.A., Keil, R.G., Devol, A.H. 2002. Impact of suboxia on sinking particulate organic carbon: Enhanced carbon flux and preferential degradation of amino acids via denitrification. Geochim et Cosmochim Acta 66, 457-465.

Ward, B.B., Glover, H.E., and Lipschultz, F. 1989. Chemoautotrophic activity and nitrification in the oxygen minimum zone off Peru. Deep Sea Res. 36, 1031-1051.

Ward, B.B., Tuit, C.B., Jayakumar, A., Rich, J.J., Moffett, J., and Naqvi, S.W.A. 2008. Organic carbon, and not copper, controls denitrification in oxygen minimum zones of the ocean. Deep Sea Res. 55, 1672-1683.

Ward, B. B., Devol, A. H., Rich, J. J., Chang, B. X., Bulow, S. E., Naik, H., Pratihary, A., Jayakumar, A. 2009. Denitrification as the dominant nitrogen loss process in the Arabian Sea. Nature 461, 78-81.

Ward, B.B. 2013. How nitrogen is lost. Science 341, 352-353.

Wyrtki, K. 1967. Circulation and Water Masses in the Eastern Equatorial Pacific Ocean. Int. J. Oceanol. & Limnol. 1, 117 – 147.

## Tables

Table 1. Calculated nitrogen isotope effects for nitrate reduction ($^{15}\varepsilon_{NAR}$) and DIN removal ($^{15}\varepsilon_{DIN\text{-}R}$) from Raleigh closed system substrate model using the sum of N pools ($[NO_3^-] + [NO_2^-] + [N_2]$), the expected N pool based on P ($[DIN]_{exp,P}$), and the OMP analysis ($[DIN]_{exp,OMP}$). The standard error is reported for each calculated ε value with the 95% CI indicated in parentheses for each ε value. The number of data points used to calculate ε (n) and the p value for the test of significance between two slopes are given for each pair of estimates. A significant difference is indicated by (*).

| | **Sum of N pools** | | **$[DIN]_{exp,P}$** | | | **$[DIN]_{exp,OMP}$** | | | |
|---|---|---|---|---|---|---|---|---|---|
| **$NO_3^-$ reduction** | **$^{15}\varepsilon_{NAR}$** | **$r^2$** | **$^{15}\varepsilon_{NAR}$** | **$r^2$** | **p value** | **$^{15}\varepsilon_{NAR}$** | **$r^2$** | **p value** | **n** |
| $26.2 < \sigma_\theta \leq 26.3$ | 18.5 ± 2.1 (5.4) | 0.97 | 17.7 ± 2.0 (5.1) | 0.97 | 0.78 | 18.4 ± 1.5 (3.9) | 0.98 | 0.97 | 7 |
| $26.3 < \sigma_\theta \leq 26.4$ | 24.9 ± 3.0 (7.3) | 0.96 | 19.5 ± 1.1 (2.7) | 0.99 | 0.12 | 22.4 ± 0.9 (2.2) | 0.99 | 0.44 | 8 |
| $26.4 < \sigma_\theta \leq 26.5$ | 23.2 ± 2.3 (5.6) | 0.97 | 20.1 ± 2.4 (5.9) | 0.96 | 0.37 | 21.3 ± 1.3 (3.2) | 0.99 | 0.49 | 8 |
| $26.5 < \sigma_\theta \leq 26.6$ | 34.6 ± 2.9 (6.6) | 0.97 | 26.6 ± 2.1 (4.8) | 0.98 | **0.04*** | 30.5 ± 1.0 (2.3) | 0.99 | 0.20 | 11 |
| $26.6 < \sigma_\theta \leq 26.7$ | 33.2 ± 2.7 (6.6) | 0.98 | 28.3 ± 3.3 (8.1) | 0.96 | 0.27 | 30.1 ± 2.4 (5.9) | 0.98 | 0.41 | 8 |
| $26.7 < \sigma_\theta \leq 26.8$ | 30.5 ± 1.1 (3.5) | 0.99 | 29.3 ± 2.4 (7.6) | 0.99 | 0.66 | 34.4 ± 8.4 (26.7) | 0.92 | 0.66 | 5 |
| **$NO_3^-$ reduction** | **$^{18}\varepsilon_{NAR}$** | **$r^2$** | **$^{18}\varepsilon_{NAR}$** | **$r^2$** | **p value** | **$^{18}\varepsilon_{NAR}$** | **$r^2$** | **p value** | **n** |
| $26.2 < \sigma_\theta \leq 26.3$ | 15.8 ± 1.9 (4.9) | 0.96 | 15.5 ± 1.3 (3.3) | 0.98 | 0.90 | 15.6 ± 0.7 (1.8) | 0.99 | 0.92 | 7 |
| $26.3 < \sigma_\theta \leq 26.4$ | 18.5 ± 3.4 (8.3) | 0.86 | 15.2 ± 1.9 (4.6) | 0.96 | 0.41 | 17.3 ± 2.2 (5.4) | 0.96 | 0.77 | 8 |
| $26.4 < \sigma_\theta \leq 26.5$ | 17.7 ± 2.6 (6.4) | 0.94 | 15.8 ± 1.9 (4.6) | 0.96 | 0.57 | 16.7 ± 1.1 (2.7) | 0.99 | 0.73 | 8 |
| $26.5 < \sigma_\theta \leq 26.6$ | 28.9 ± 4.3 (9.7) | 0.92 | 23.5 ± 1.5 (1.1) | 0.98 | 0.25 | 25.2 ± 2.4 (5.4) | 0.96 | 0.46 | 11 |
| $26.6 < \sigma_\theta \leq 26.7$ | 29.5 ± 2.9 (7.1) | 0.97 | 16.1 ± 1.3 (3.2) | 0.99 | **0.001*** | 26.4 ± 3.2 (7.8) | 0.96 | 0.47 | 8 |
| $26.7 < \sigma_\theta \leq 26.8$ | 42.0 ± 19.6 (60) | 0.78 | 46.5 ± 15.0 (47.7) | 0.87 | 0.86 | 52 ± 15.6 (49.6) | 0.89 | 0.70 | 5 |
| **DIN reduction** | **$^{15}\varepsilon_{DIN\text{-}R}$** | **$r^2$** | **$^{15}\varepsilon_{DIN\text{-}R}$** | **$r^2$** | **p value** | **$^{15}\varepsilon_{DIN\text{-}R}$** | **$r^2$** | **p value** | **n** |
| $26.2 < \sigma_\theta \leq 26.3$ | 8.6 ± 3.8 (9.8) | 0.71 | 9.5 ± 0.7 (1.8) | 0.99 | 0.82 | 10.3 ± 1.1 (2.8) | 0.97 | 0.74 | 7 |
| $26.3 < \sigma_\theta \leq 26.4$ | 19.2 ± 5.1 (12.4) | 0.84 | 13.2 ± 1.5 (3.7) | 0.96 | 0.28 | 17.3 ± 2.0 (4.9) | 0.96 | 0.73 | 8 |
| $26.4 < \sigma_\theta \leq 26.5$ | 7.8 ± 5.4 (13.2) | 0.51 | 7.5 ± 3.7 (9.1) | 0.64 | 0.96 | 8.3 ± 4.9 (12) | 0.57 | 0.95 | 8 |
| $26.5 < \sigma_\theta \leq 26.6$ | 31.3 ± 6.7 (15.2) | 0.85 | 18.4 ± 1.1 (2.5) | 0.98 | 0.07 | 27.4 ± 2.7 (6.1) | 0.96 | 0.59 | 11 |

| | | | | | | | | | |
|---|---|---|---|---|---|---|---|---|---|
| $26.6 < \sigma_\theta \leq 26.7$ | 35.8 ± 7.6 (18.6) | 0.89 | 20.2 ± 5.4 (13.2) | 0.84 | 0.12 | 31.1 ± 8.0 (19.6) | 0.85 | 0.68 | 8 |
| $26.7 < \sigma_\theta \leq 26.8$ | 3.5 ± 15.4 (49) | 0.13 | 24.5 ± 3.5 (11.1) | 0.97 | 0.23 | 10.2 ± 4.5 (14.3) | 0.8 | 0.69 | 5 |

Table 2. Summary of model scenarios used to explore the mechanisms affecting apparent $^{15}\varepsilon_{NAR}$ and $^{15}\varepsilon_{DIN\text{-}R}$

| Parameter /Scenario | I | II | III | IV | V | VI | VII | VIII | IX | X |
|---|---|---|---|---|---|---|---|---|---|---|
| $k_{NXR}$ ($year^{-1}$) | 0 | 0 | 0.5 | 1 | 0.5 | 0 | 0 | 0.5 | 0 | 0.5 |
| $k_{NIR}$ ($year^{-1}$) | 0.5 | 1 | 0.5 | 1 | 0 | 2 | 0.5 | 0.5 | 0.5 | 0.5 |
| $k_{NAR}$ ($year^{-1}$) | 0.5 | 0.5 | 0.5 | 0.5 | 0.5 | 0.5 | 0.5 | 0.5 | 0.5 | 0.5 |
| $^{15}\varepsilon_{NAR}$ (‰) | 12 | 12 | 12 | 12 | 12 | 12 | 12 | 12 | 25 | 25 |
| $^{15}\varepsilon_{NIR}$ (‰) | 0 | 0 | 0 | 0 | 0 | 0 | 10 | 0 | 0 | 0 |
| $^{15}\varepsilon_{NXR}$ (‰) | -32 | -32 | -32 | -32 | -32 | -32 | -32 | -13 | -32 | -32 |
| Maximum $[NO_2^-]$ (μM) | 15.5 | 10.8 | 11.6 | 7.3 | 20.1 | 7.0 | 15.5 | 11.6 | 15.5 | 11.6 |
| Apparent $^{15}\varepsilon_{NAR}$ (‰) | 13.0 | 13.0 | 25.6 | 27.7 | 38.1 | 13.0 | 13.0 | 15.8 | 27.7 | 35.9 |
| Apparent $^{15}\varepsilon_{DIN\text{-}R}$ (‰) | 8.3 | 12.2 | 23.3 | 27.0 | NA[a] | 12.9 | 15.3 | 14.8 | 17,4 | 33.2 |

[a]Not applicable (NA) because in scenario V there was no change in [DIN] or $\delta^{15}N_{DIN}$.

**Figure Legends**

Figure 1. Map of the cruise track, with station numbers. Stations included in 'section A' are located within the green box, while stations included in 'section B' are located within the red box. Asterisks indicate stations where $[N_2]_{bio}$ measurements where collected.

Figure 2. Concentrations of $NO_2^-$ (A and B) and $O_2$ (C and D), with contours of potential density ($\sigma_\theta$). $[DIN]_{def,P}$ ($[DIN]_{def,P} = 15.8*([PO_4^{3-}] - 0.3) - ([NO_2^-] + [NO_3^-])$) is shown in the bottom panels (E and F). All panels on the left side of the figure are from stations along section A, and all panels on the right side of the figure are from stations along section B (beginning in the north with station 8). Asterisks indicate stations where $[N_2]_{bio}$ was measured.

Figure 3. Profiles of observed, background, and water mass end member values of dissolved $O_2$ (A), $NO_3^-$ (B), and $PO_4^{3-}$ (C) versus potential density anomaly. Solid lines indicate ESSW end member values, dashed lines indicated ESPIW end member values, white diamonds indicate background concentrations, and gray circles indicate the observations. In panel (D), the calculated amount of $[NO_3^-]$ added by $O_2$ remineralization ($[NO_3^-]_{remin}$) is shown by the black circles which is used to calculate the expected DIN pool calculated through OMP analysis (gray squares). The expected DIN pool calculated from $[PO_4^{3-}]$ measurements is indicated by white triangles.

Figure 4. Concentration measurements of biogenic $N_2$ (triangles), calculated DIN deficit based on P ($[DIN]_{def,P}$; solid lines), and DIN deficit based on OMPA ($[DIN]_{def,OMP}$; dashed lines). Panels A through I show data from stations 8, 9, 11, 14, 17, 18, 19, BB1, and BB2, respectively.

Figure 5. Comparison of measured $[N_2]_{bio}$ vs. $[DIN]_{def,P}$ (open circles) and $[DIN]_{def,OMP}$ (filled circles). Regressions for $[N_2]_{bio}$ vs. $[DIN]_{def,P}$ shown in dashed line (slope = 0.75 ± 0.05) and regression for $[N_2]_{bio}$ vs. $[DIN]_{def,OMP}$ shown with solid line (slope =1.01 ± 0.06).

Figure 6. $\delta^{15}N$ and $\delta^{18}O$ of $NO_3^-$ along section A (panels A and C) and section B (panels B and D). Panel organization is the same as that in Figure 2. Contours of potential density ($\sigma_\theta$) are indicated by the solid black lines.

Figure 7. Measured $\delta^{15}N$ values of $NO_2^-$ (green circles), $NO_3^-$ (blue squares), and biogenic $N_2$ (red triangles) from stations where $\delta^{15}N_{N2,bio}$ data is available. Error bars on $\delta^{15}N_{N2,bio}$ indicate measurement error. The dashed red lines denote the range in $\delta^{15}N_{N2,bio}$ values that result when the background $\delta^{15}N_{N2}$ is allowed to vary between 0.68‰ and 0.72‰. The dashed black lines indicate the concentration of dissolved $O_2$ (bottom x-axis in each panel). Concentrations of $NO_2^-$ at stations 8 and 19 were below the minimum threshold required for isotope analysis ($[NO_2^-]$ must be > 0.25 μM), and thus no $\delta^{15}N_{NO2}$ data is available at those stations.

Figure 8. Time course concentration and isotope data from model scenarios I (A and B) and II (C and D). Concentrations (A and C) and isotopes (B and D) of $NO_2^-$ are shown with red dotted lines, $NO_3^-$ with blue dashed lines, DIN with solid black line, and $N_2$ with green dot-dashed lines.

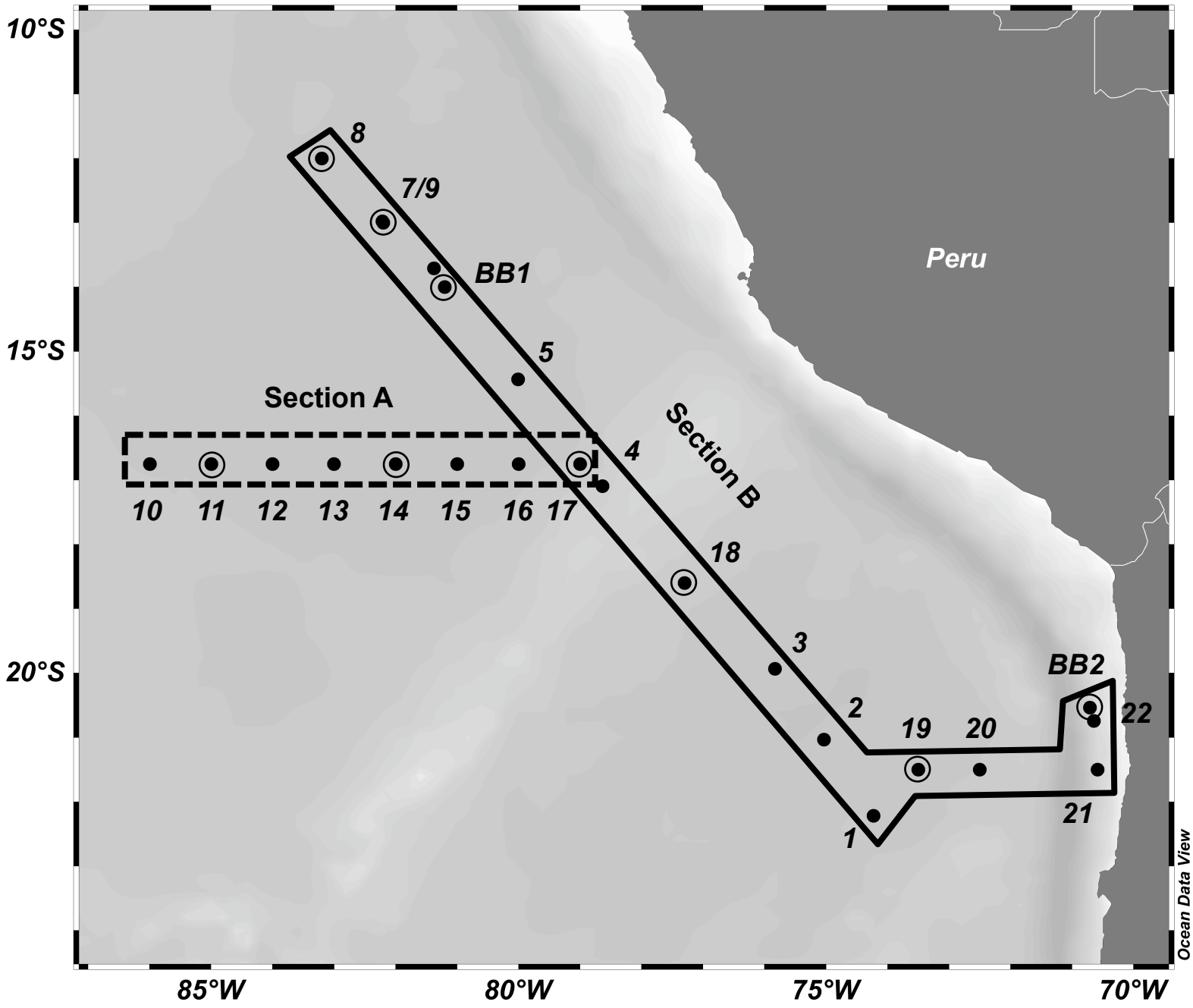
10°S
15°S
20°S
85°W
80°W
75°W
70°W
Peru
Section A
Section B
8
7/9
BB1
5
4
10
11
12
13
14
15
16
17
18
3
2
1
BB2
19
20
21
22
Ocean Data View

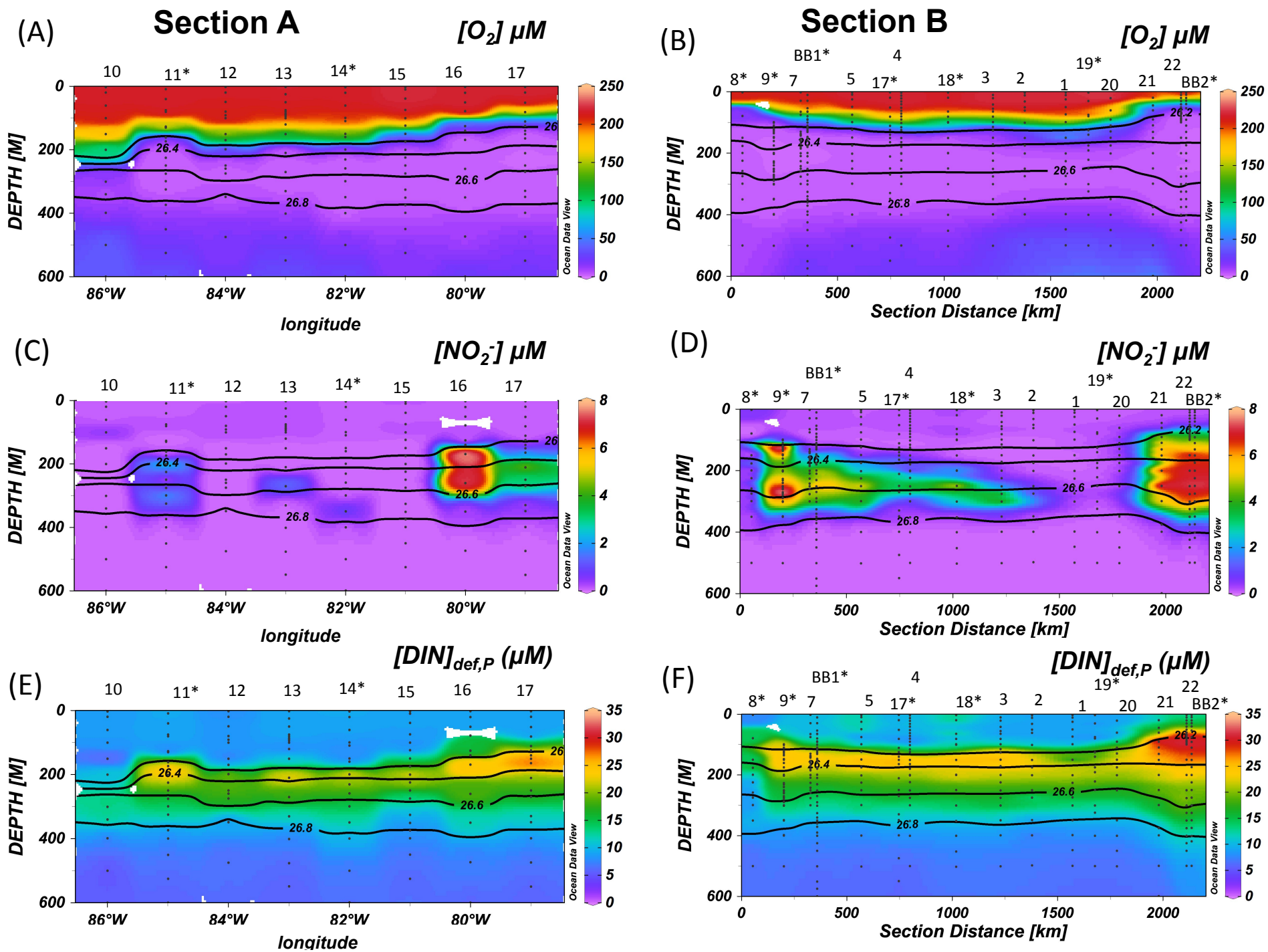
(A)
Section A
[O2] µM
10
11*
12
13
14*
15
16
17
DEPTH [M]
0
200
400
600
26
26.4
26.6
26.8
86°W
84°W
82°W
80°W
longitude
Ocean Data View
250
200
150
100
50
0
(B)
Section B
[O2] µM
BB1*
4
8*
9*
7
5
17*
18*
3
2
19*
1
20
21
22
BB2*
26.2
0
500
1000
1500
2000
Section Distance [km]
(C)
[NO2-] µM
8
6
4
2
0
(D)
[NO2-] µM
(E)
[DIN]def,P (µM)
35
30
25
20
15
10
5
0
(F)
[DIN]def,P (µM)

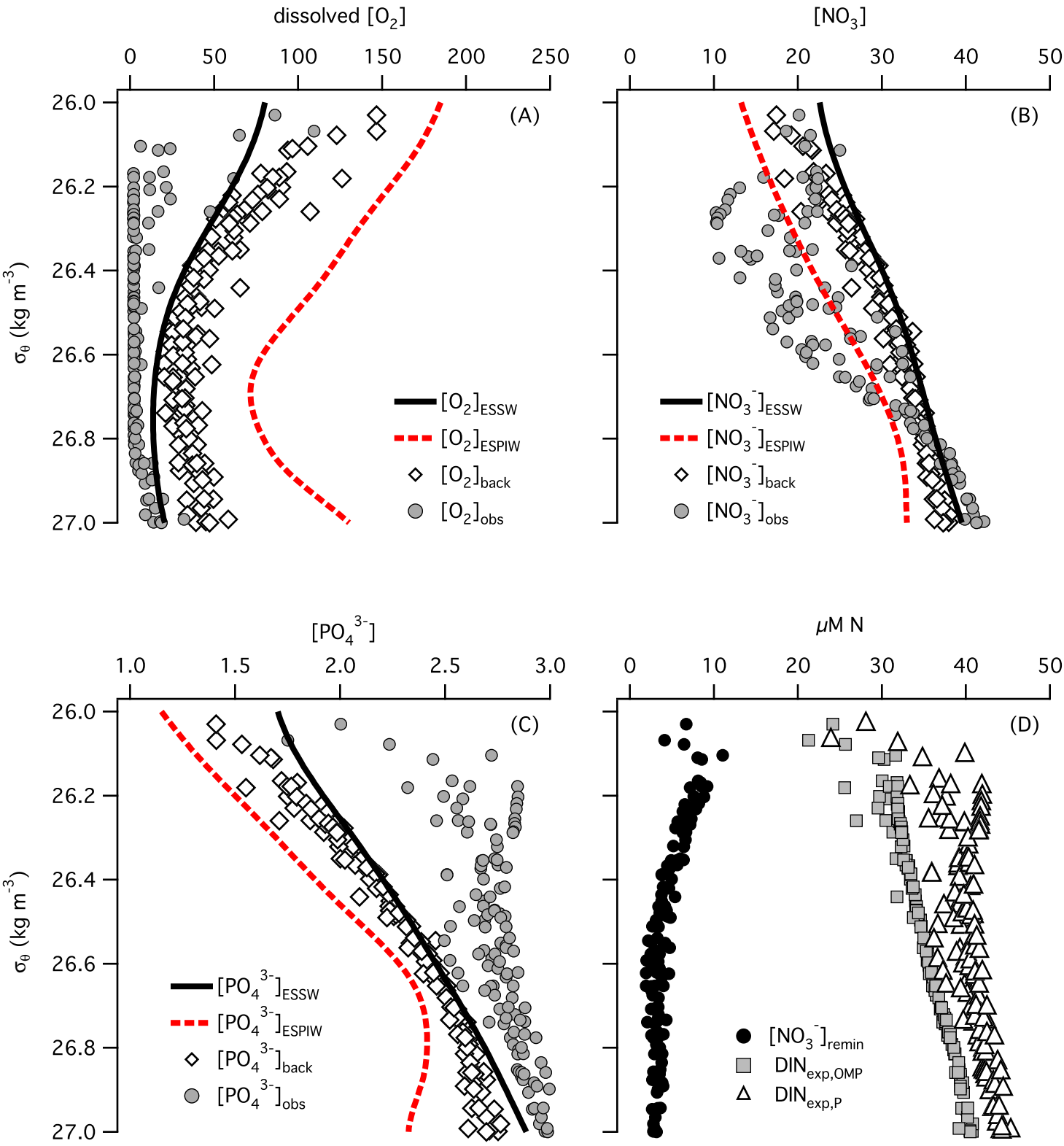
dissolved [O2]
0
50
100
150
200
250
(A)
[O2]ESSW
[O2]ESPIW
[O2]back
[O2]obs
[NO3]
0
10
20
30
40
50
(B)
[NO3-]ESSW
[NO3-]ESPIW
[NO3-]back
[NO3-]obs
σθ (kg m-3)
26.0
26.2
26.4
26.6
26.8
27.0
[PO43-]
1.0
1.5
2.0
2.5
3.0
(C)
[PO43-]ESSW
[PO43-]ESPIW
[PO43-]back
[PO43-]obs
μM N
0
10
20
30
40
50
(D)
[NO3-]remin
DINexp,OMP
DINexp,P

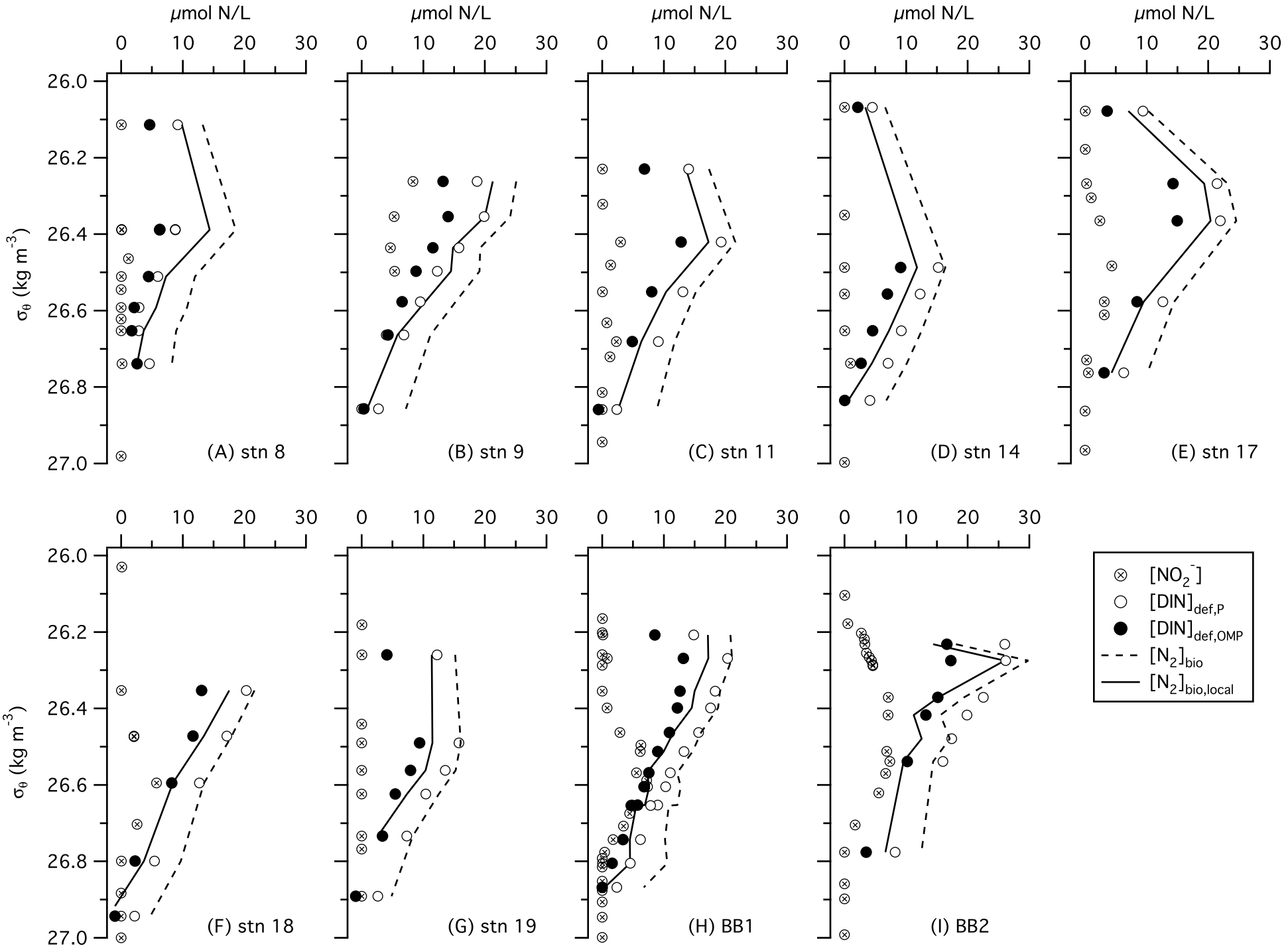
μmol N/L
0
10
20
30
26.0
26.2
26.4
26.6
26.8
27.0
σθ (kg m-3)
(A) stn 8
(B) stn 9
(C) stn 11
(D) stn 14
(E) stn 17
(F) stn 18
(G) stn 19
(H) BB1
(I) BB2
[NO2-]
[DIN]def,P
[DIN]def,OMP
[N2]bio
[N2]bio,local

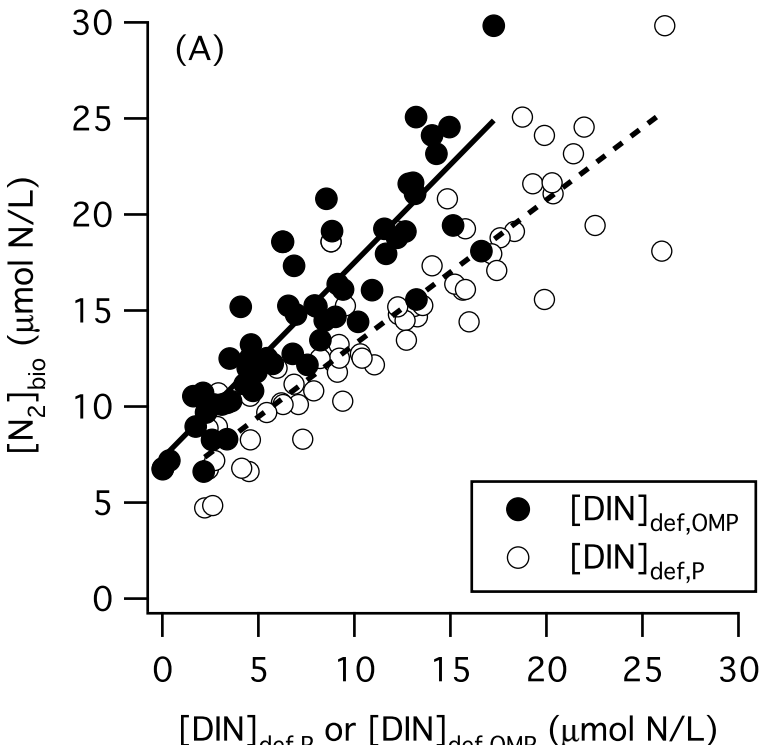
(A)
30
25
20
15
10
5
0
0
5
10
15
20
25
30
[N2]bio (µmol N/L)
[DIN]def,P or [DIN]def,OMP (µmol N/L)
[DIN]def,OMP
[DIN]def,P

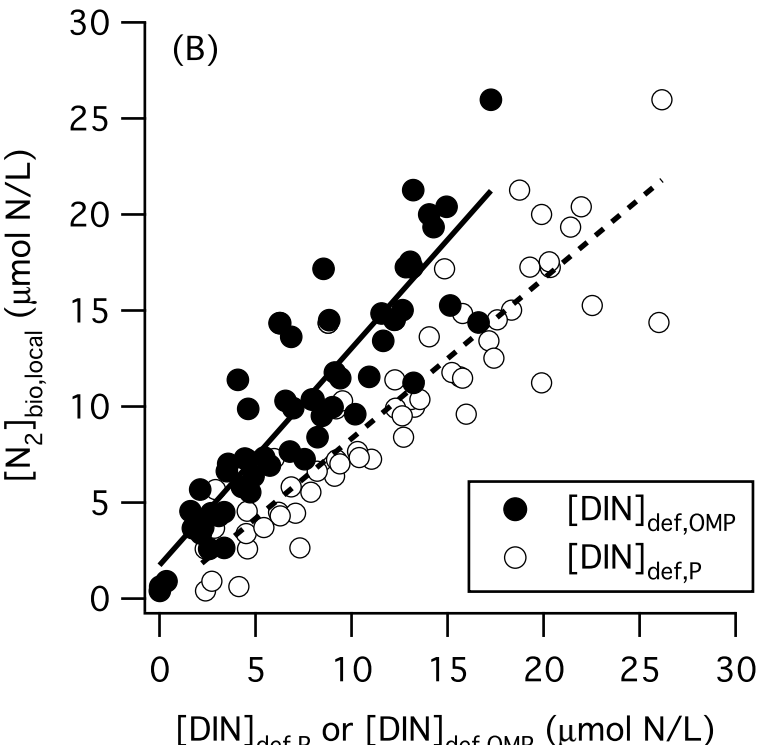
(B)
30
25
20
15
10
5
0
0
5
10
15
20
25
30
[N2]bio,local (µmol N/L)
[DIN]def,P or [DIN]def,OMP (µmol N/L)
[DIN]def,OMP
[DIN]def,P

## Section A

## Section B

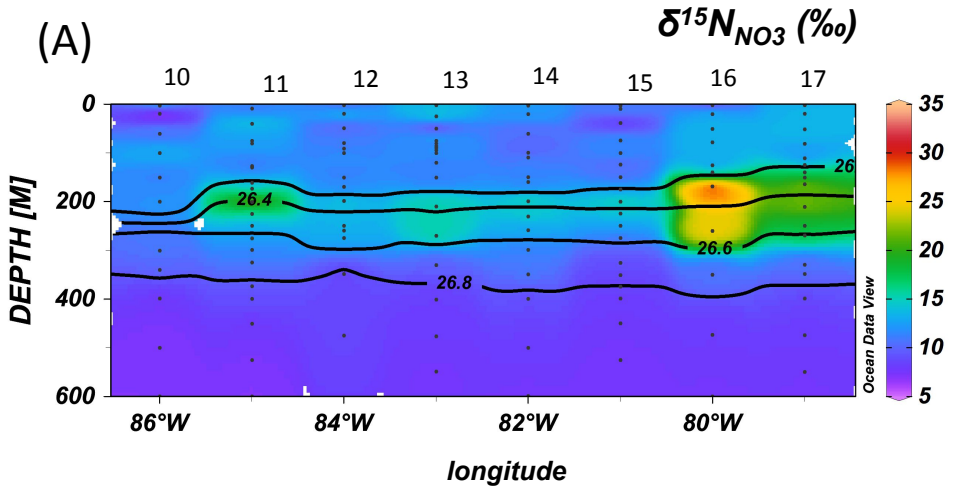


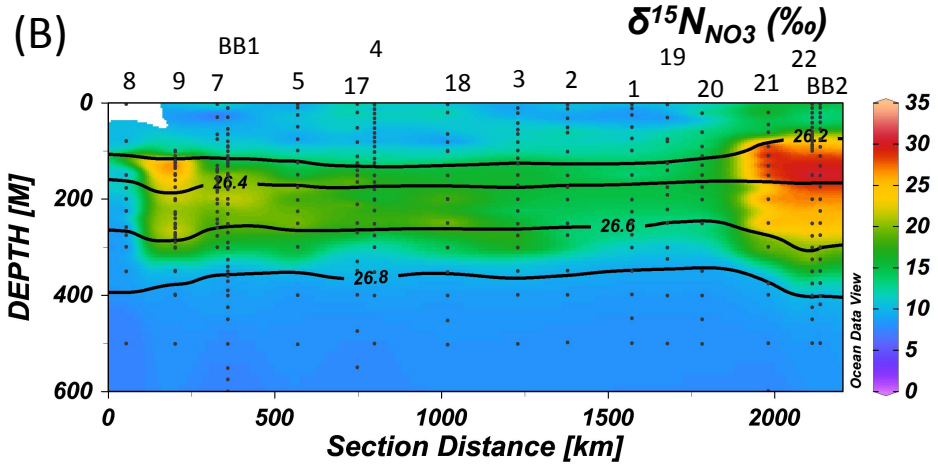


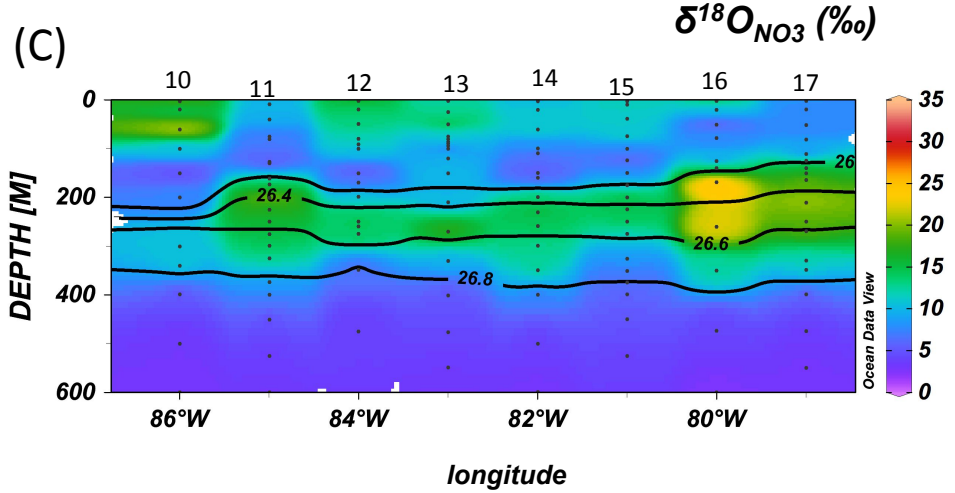


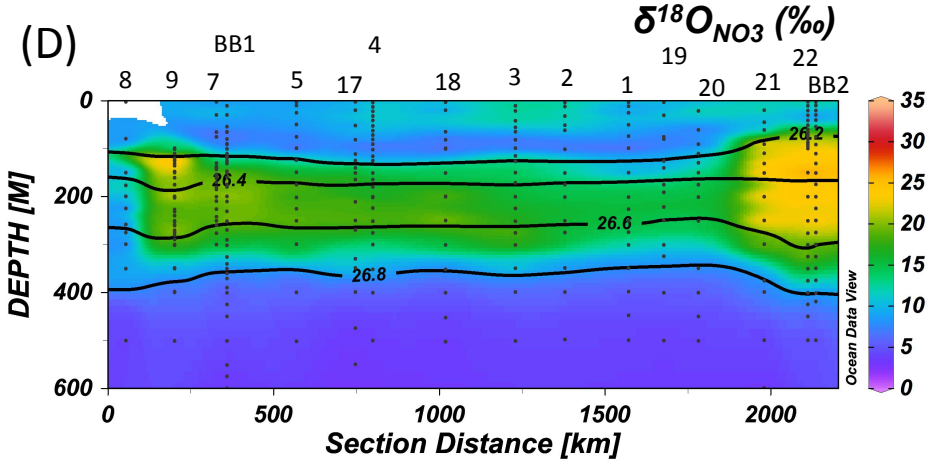

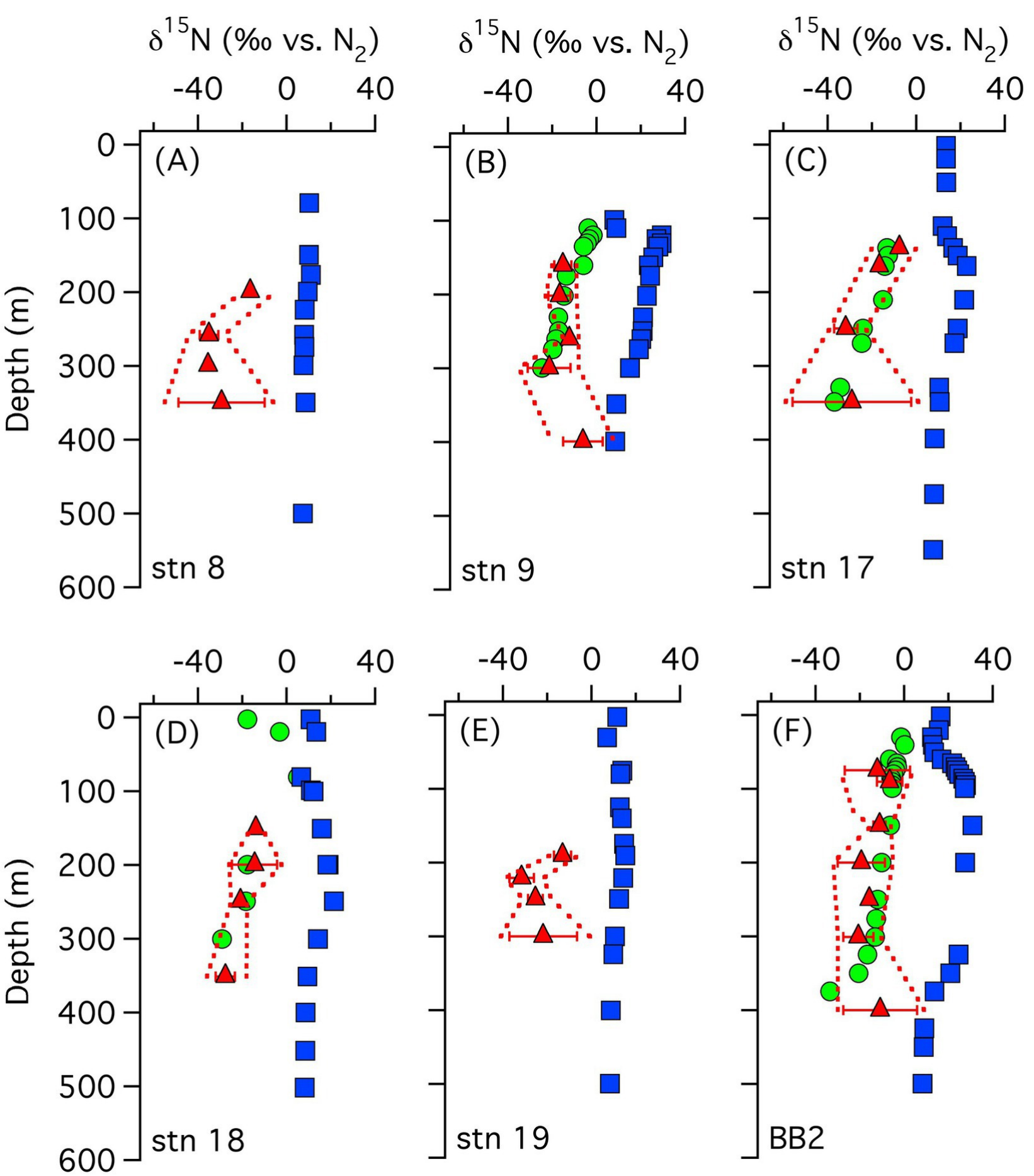
δ15N (‰ vs. N2)
-40
0
40
Depth (m)
0
100
200
300
400
500
600
(A)
stn 8
(B)
stn 9
(C)
stn 17
(D)
stn 18
(E)
stn 19
(F)
BB2

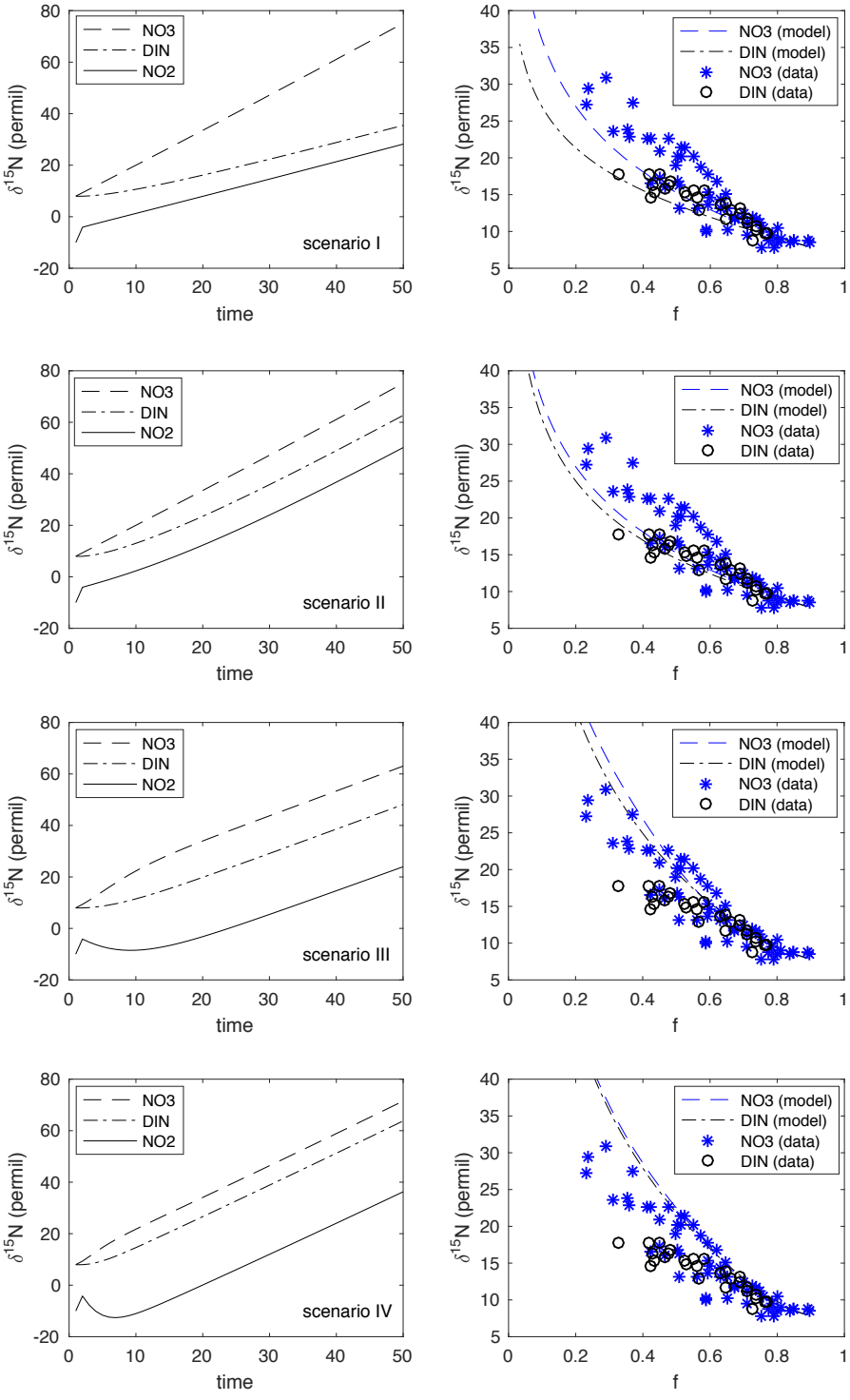
NO3
DIN
NO2
scenario I
scenario II
scenario III
scenario IV
time
f
δ15N (permil)
NO3 (model)
DIN (model)
NO3 (data)
DIN (data)